Title
Synthesis and structural properties of a 2D Zn(II) dodecahydroxy-*closo*-dodecaborate coordination polymer

Journal
Dalton Transactions, 51(30)

ISSN
1477-9226 1477-9234

Authors
Ready, Austin D
Becwar, Shona M
Jung, Dahee
et al.

Publication Date
2022

DOI
10.1039/D2DT01292H

Peer reviewed

ARTICLE

Synthesis and structural properties of a 2D Zn(II) dodecahydroxy-*closo*-dodecaborate coordination polymer

Austin D. Ready†[a], Shona M. Becwar†[e], Dahee Jung[a,b], Anna Kallistova[c], Emily Schueller[c], Kierstyn P. Anderson[a,b], Rebecca Kubena[a], Ram Seshadri[c,d], Bradley F. Chmelka*[e], Alexander M. Spokoyny*[a,b]

In this work, we discuss the synthesis and characterization of a 2D coordination polymer composed of a dianionic perhydroxylated boron cluster, $[B_{12}(OH)_{12}^{2-}]$, coordinated to Zn(II)—the first example of a transition metal-coordinated $[B_{12}(OH)_{12}]^{2-}$ compound. This material was synthesized via cation exchange from the starting cesium salt and then subjected to rigorous characterizion prior to and after thermal activation. Numerous techniques, including XRD, FTIR, SEM, TGA, and solid-state NMR revealed a 2D coordination polymer composed of sheets of Zn(II) ions intercalated between planes of boron clusters. The as-synthesized material was then evacuated of solvent via thermal treatment, and atomic-level changes from this transformation were elucidated through a combination of 1D and 2D solid-state NMR analyses of ^{11}B and ^{1}H nuclei, suggesting the full removal of coordinated solvent molecules. Evidence also suggested that $[B_{12}(OH)_{12}^{2-}]$ can adjust its coordination to Zn(II) in the solid-state through hemilability of its numerous -OH ligands.

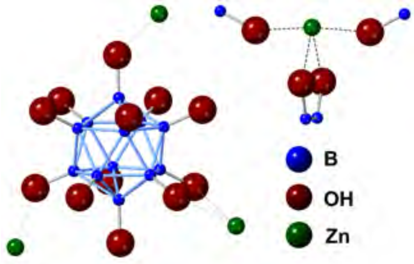

Introduction

Coordination polymers are an exciting class of materials featuring a high degree of chemical tunability due to the enormous variety of molecular building blocks available.[1-3] Among these, boron rich clusters have been recently introduced as promising scaffolds for the construction of various types of coordination networks.[4-31] In general, polyhedral boron clusters (Scheme 1) are highly appealing as building blocks for structured materials due to their symmetry, chemical tunability, and thermal/chemical robustness arising from a three-dimensional delocalization of electron density.[4-10, 32, 33] Notably, Stang et al. explored the use of carboranes (Scheme 1)—neutral twelve-membered boron clusters in which two vertices have been replaced with carbon atoms—as linkers to form metal-coordinated networks,[11, 17] among other early examples of using

---

[a] Department of Chemistry and Biochemistry, University of California, Los Angeles, Los Angeles, CA, USA.
[b] California NanoSystems Institute (CNSI), University of California, Los Angeles, Los Angeles, CA, USA
[c] Materials Department and Materials Research Laboratory, University of California, Santa Barbara, Santa Barbara, CA, USA
[d] Department of Chemistry and Biochemistry, University of California, Santa Barbara, Santa Barbara, CA, USA
[e] Department of Chemical Engineering, University of California, Santa Barbara, Santa Barbara, CA, USA

†These authors contributed equally
*bradc@ucsb.edu
*spokoyny@chem.ucla.edu

Electronic Supplementary Information (ESI) available: Atomic coordinates, crystallographic information file, density functional theory calculations, etc. See DOI: 10.1039/x0xx00000x

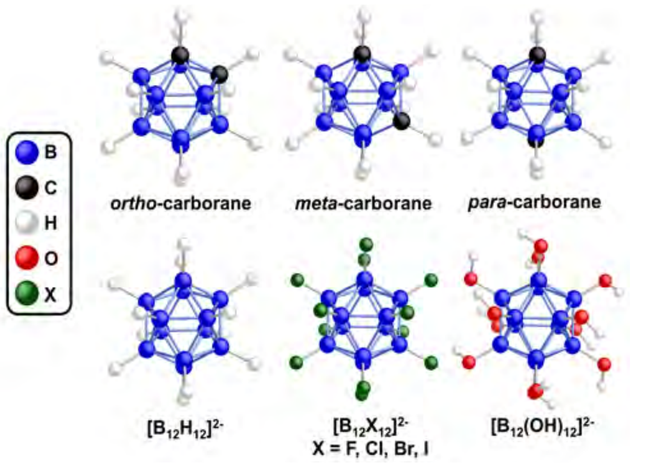

Scheme 1 Icosahedral boron clusters studied thus far as metal-coordinating moieties.

carborane clusters to form coordination polymers.[29, 31] Compared to purely boron-containing clusters, the presence of two carbon atoms in carboranes engenders an inherent directionality to the cluster through disruption of the symmetrical electronic environment. Shortly thereafter, Hupp, Mirkin, and co-workers reported the syntheses of Zn(II) and Co(II) carborane-containing MOFs.[12, 13, 25] Additionally, Planas et al. published a series of papers[14, 15, 23, 26, 27] investigating a number of carborane-based MOFs and coordination polymers. These works showcased the ability of boron clusters which are functionalized with various substituents (Scheme 1) to be used as hybrid building blocks for the formation of coordination polymer networks. Of particular interest is the coordination ability of purely boron-containing clusters such as dianionic dodecaborate—$[B_{12}H_{12}]^{2-}$. In 1964, Muetterties demonstrated that due to the highly delocalized bonding in dodecaborate, the dicesium salt ($Cs_2B_{12}H_{12}$) can withstand temperatures up to 650°C without significant thermal decomposition, as well as exposure to strong acids and bases.[34] Furthermore, $[B_{12}H_{12}]^{2-}$ is also amenable to functionalization, as evident by the variety of perhalogenated derivatives ($[B_{12}X_{12}]^{2-}$; X= F, Cl, Br, I) synthesized by Knoth, Muetterties, and others in subsequent years.[35-37] These halogenated clusters and their derivatives have since been studied due to their ability to act as highly inert, weakly coordinating anions.[38-48] A notable example from Strauss et al. showed a thorough solid-state characterization of $Na_2B_{12}X_{12}$ compounds (X = F, Cl) and the corresponding hydrates.[49] By comparing the Na—O bond valence contributions of the hydrates, the authors were able to rank these halogenated derivatives with respect to dodecaborate in terms of relative coordinating ability towards Na^+ ions in the solid state ($B_{12}Cl_{12}^{2-} \ll B_{12}H_{12}^{2-} < B_{12}F_{12}^{2-}$).

Recently, Xing and Duttwyler used an electrophilic metal ion in combination with an unfunctionalized $[B_{12}H_{12}]^{2-}$ building block to create the first porous boron cluster-containing network where the coordination is driven purely by direct cage-metal interactions.[30] Notably, the authors observed a linear B—H···M interaction (M = Cu(II)), a previously unrecognized bonding motif for a metal dodecaborate complex, as the boron cluster typically coordinates to metal centers with two or three B-H units.[50-53] We hypothesized that a perhydroxylated dodecaborate cluster,[21, 22, 54] where instead of -H groups the icosahedral boron cluster core features twelve -OH groups (i.e. $[B_{12}(OH)_{12}]^{2-}$) could be an interesting building block with which to create a coordination polymer. For example, we previously reported[19] the synthesis of a hybrid metal oxide system, wherein $[B_{12}(OH)_{12}]^{2-}$ was used as a starting material to form a cross-linked network featuring B—O—Ti linkages connecting an amorphous array of TiO_2 nanoparticles. We later expanded this chemistry to synthesize a boron-rich hybrid tungsten oxide material.[18] Additionally, the synthesis and crystallographic characterization of a number of alkali metal $M_2[B_{12}(OH)_{12}]$ compounds has been reported[16, 20-22, 24, 28, 54] (M = Li, Na, K, Rb, Cs). Despite reports of Zn(II)-boron cluster coordination compounds,[55] however, to date there remain no reports of the synthesis and characterization of a crystalline, perhydroxylated dodecaborate coordination polymer with a cation other than a monovalent alkali metal.

Herein, we present the synthesis and characterization of $ZnB_{12}(OH)_{12}$, a 2D coordination polymer composed of planes of divalent Zn(II) ions coordinated by $[B_{12}(OH)_{12}]^{2-}$ units, the first example of a transition metal-coordinated $[B_{12}(OH)_{12}]^{2-}$ compound. We report a facile synthesis as well as a thorough investigation of the change in chemical environment of the cluster upon high temperature solvent removal, as determined via XRD refinement and ^1H-^{11}B and ^1H-^1H solid-state 2D NMR studies of the as-synthesized and activated materials.

Experimental

Synthesis of $ZnB_{12}(OH)_{12}$

$Cs_2[B_{12}(OH)_{12}]$ (120 mg, 0.20 mmol) was added to a 20 mL reaction tube. MilliQ water (3.0 mL) was added. The suspension was heated to 95 °C until all $Cs_2[B_{12}(OH)_{12}]$ was dissolved. A solution of $Zn(NO_3)_2 \bullet 6H_2O$ (714 mg, 2.4 mmol) in MilliQ water (3.0 mL) was prepared at room temperature and added dropwise to the homogenous $Cs_2[B_{12}(OH)_{12}]$ solution. Upon addition, a crystalline white precipitate formed immediately (Fig. 1). The suspension was stirred at 95 °C for two days. After completion, the suspension was cooled to room temperature, and was centrifuged (2000 rpm, 10 minutes) to separate the solids. The top aqueous solution was decanted. Another portion of MilliQ water (15.0 mL) was added. The suspension was stirred in an ice-water bath for 5 min, and centrifuged (2000 rpm, 5 minutes) to separate the solids. This washing step was repeated another two times to remove soluble impurities. The resulting white powder was dried in vacuo with a lyophilizer for one day to yield the final product (65 mg, 0.162 mmol, 81%). The material was activated by heating *in vacuo* at 220°C for 24 hours.

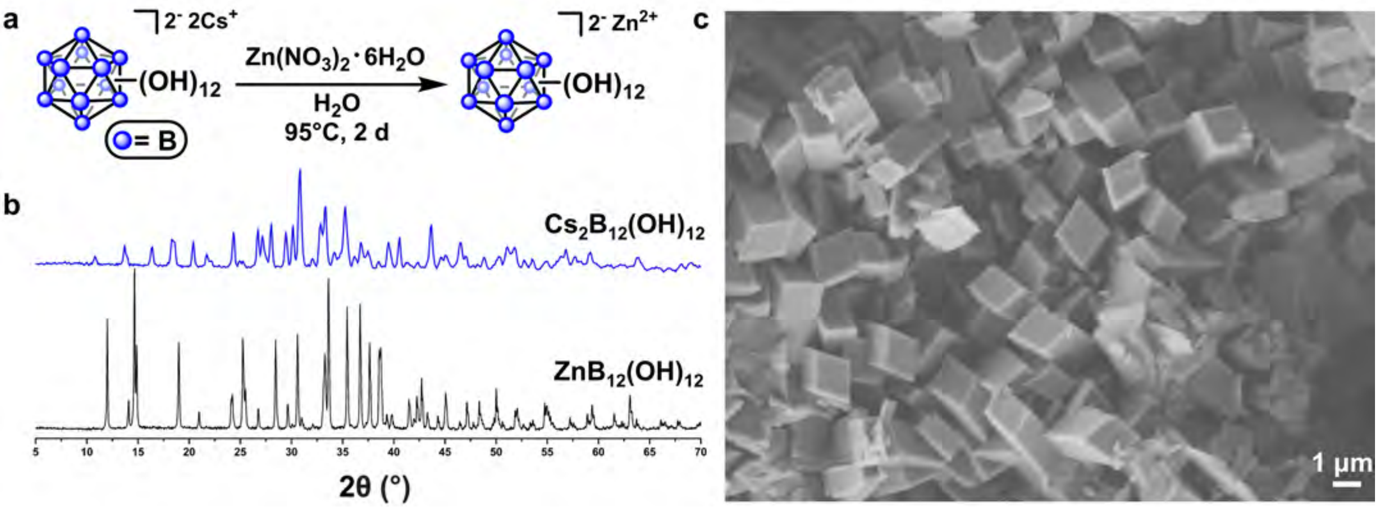

Fig. 1 (a) Synthetic conditions to perform cation exchange on perhydroxylated dodecaborate. (b) PXRD pattern of as-synthesized boron cluster before (blue) and after cation exchange (black) from cesium to zinc. (c) SEM image of as-synthesized $ZnB_{12}(OH)_{12}$, showcasing the high degree of crystallinity and uniformity.

X-ray crystallography and structure determination

XRD patterns (Fig. 1b and Fig. 3b) were collected on a ground sample of $ZnB_{12}(OH)_{12}$ from 5 to 120° (2θ) on an Empyrean diffractometer with Cu-Kα radiation (λ = 1.54 Å). The powder pattern was indexed using the EXPO2014 software with the N-TREOR09 indexing algorithm to obtain a unit cell with *P*–1 symmetry. This unit cell was put into TOPAS, along with the diffraction data, and a Pawley fit was performed to obtain refined cell, background, profile (peak shape), and sample displacement parameters. Bond lengths and angles for the $[B_{12}(OH)_{12}]^{2-}$ moiety were obtained from the single crystal structure of the dicesium salt[54]. These parameters were fixed and information about the atoms was imported into TOPAS. The boron clusters were fixed in shape as rigid bodies with the -OH groups on both the boron cluster and the solvent replaced by F atoms for simplicity (Fig. S10 and S11). The clusters were allowed to rotate and translate, as well as the zinc ions and fluorine atoms. A simulated annealing algorithm was implemented in TOPAS which varied the atom positions in order to minimize the least squared error from the XRD pattern. When the cell parameters were also allowed to vary the cell relaxed into monoclinic symmetry. FINDSYM was used on the resulting structure to obtain the new space group, which was monoclinic *C*2/*m*. Simulated annealing was performed on the new monoclinic structure to obtain the best fit to the XRD pattern. Finally, a Rietveld refinement was performed in order to obtain atomic displacement parameters and statistical information about the quality of the fit (Table S1 and S2). Because β is close to 90°, the Rietveld refinement was attempted using a variety of orthorhombic space groups following the above method. However, the best fit was achieved with monoclinic C2/*m*.

Solid-state NMR spectroscopy

Solid-state ^{1}H and ^{11}B magic-angle-spinning (MAS) NMR spectroscopy were used to analyze the local environments of ^{1}H and ^{11}B in the as-synthesized and activated boron clusters. All solid-state NMR spectra were acquired on a Bruker AVANCE II HD 800 NMR spectrometer with an 18.8 T superconducting magnet operating at Larmor frequencies of 800.24 and 256.75 MHz for ^{1}H and ^{11}B nuclei, respectively, and equipped with a fast MAS 1.3 mm HX probe head. The experiments were conducted using zirconia rotors with Kel-F® caps at 25 kHz MAS and at room temperature, which was maintained by cooling. ^{1}H chemical shifts were referenced to TKS as a secondary standard (^{1}H chemical shift of 0.25 ppm), and ^{11}B signals were referenced to borax powder ($Na_2B_4O_7$) as a secondary standard (^{11}B shift of 2.26 ppm).[56] The materials were diluted with KBr at a sample:KBr ratio of 1:1 w/w before being loaded into the MAS rotor. The KBr served as both an internal temperature probe[57] and to reduce undesirable sample heating that may arise from rapid rotation of conductive samples in the high magnetic field required for the NMR measurements.[58] Compared to 1D NMR, two-dimensional (2D) NMR techniques yield enhanced spectral resolution by exploiting through-space dipole-dipole interactions over sub-nanometer distances to correlate the NMR signals of dipole-dipole-coupled spin pairs, such as ^{1}H and ^{11}B nuclei in the boron clusters.

Solid-state 2D $^{11}B\{^{1}H\}$ Heteronuclear Correlation (HETCOR) NMR spectroscopy experiments were acquired using 32 transients, with a recycle delay of 1–5 s, 0.5 ms contact time, and 256 scans in the indirect dimension. In this experiment, ^{1}H nuclei are excited by a radiofrequency pulse, allowed to evolve during an incremented evolution period, after which polarization is transferred via ^{1}H-^{11}B dipole-dipole couplings to nearby (1 nm) ^{11}B atoms, and the ^{11}B polarization subsequently detected. A double Fourier transform of the ^{11}B and ^{1}H time-domain signals yields a contour-plot 2D frequency map of correlated ^{11}B and ^{1}H signals that manifests pairs of nuclear spins that are in nanoscale proximity to one another. Heteronuclear ^{1}H-^{11}B dipole-dipole couplings scale with the cube of the distance separating the two nuclear spins,[59, 60] so that the short contact times used were sensitive principally to ^{1}H and ^{11}B nuclei that are directly bonded, physically interacting, or, to a lesser extent, by weaker next-nearest neighbor interactions.

Solid-state 2D $^{1}H\{^{1}H\}$ double-quantum–single-quantum (DQ-SQ) NMR spectra were acquired using a Hahn-echo sequence to remove the ^{1}H background of the NMR probe head. For DQ excitation, the Back-to-Back (BaBa) scheme[61, 62] was used under MAS conditions of 25 kHz, with XY16 phase cycling[63] to remove background signals. A *z*-filter delay of 10 rotor periods was used before acquisition to remove spurious magnetization. The acquisition of the indirect dimension was rotor-synchronized, with 64 data points recorded using the States-TPPI method. Recycle delays were in the range of 1–5 s, as determined from saturation recovery measurements.

Solid-state 1D ^{1}H and ^{11}B Hahn-echo NMR experiments were conducted to quantify the integrated intensities of signals, the positions and linewidths of which are manifested in the 2D spectra. For the ^{1}H spectra, recycle delays of 20 s ($5T_1$) were used to ensure full spin-lattice relaxation of the ^{1}H signals and were acquired with 64 scans and a 0.8 ms echo delay. For the ^{11}B spectra, a recycle delay of 4 s ($>5T_1$) was used to ensure full spin-lattice relaxation of the ^{11}B signals and were acquired with 124 scans and a 0.8 ms echo delay.

Scanning Electron Microscopy

SEM images were captured with a JEOL JSM-6700F FE-SEM. The LEI detector was used with an accelerating voltage of 5.0 kV, emission current of 10 µA, and a probe current of 8 µA.

Infrared Spectroscopy

IR spectra were measured on a Jasco FT/IR-4100. A background spectrum was measured and automatically subtracted prior to sample measurements. 64 scans were used on a typical measurement.

Thermogravimetric Analysis

Thermogravimetric analysis was carried out on a PerkinElmer Pyris Diamond TG/DTA. Samples were heated in alumina oxide trays from 25 °C to 650 °C at a rate of 20 °C/min under a constant flow of argon (200 mL/min).

Results and discussion

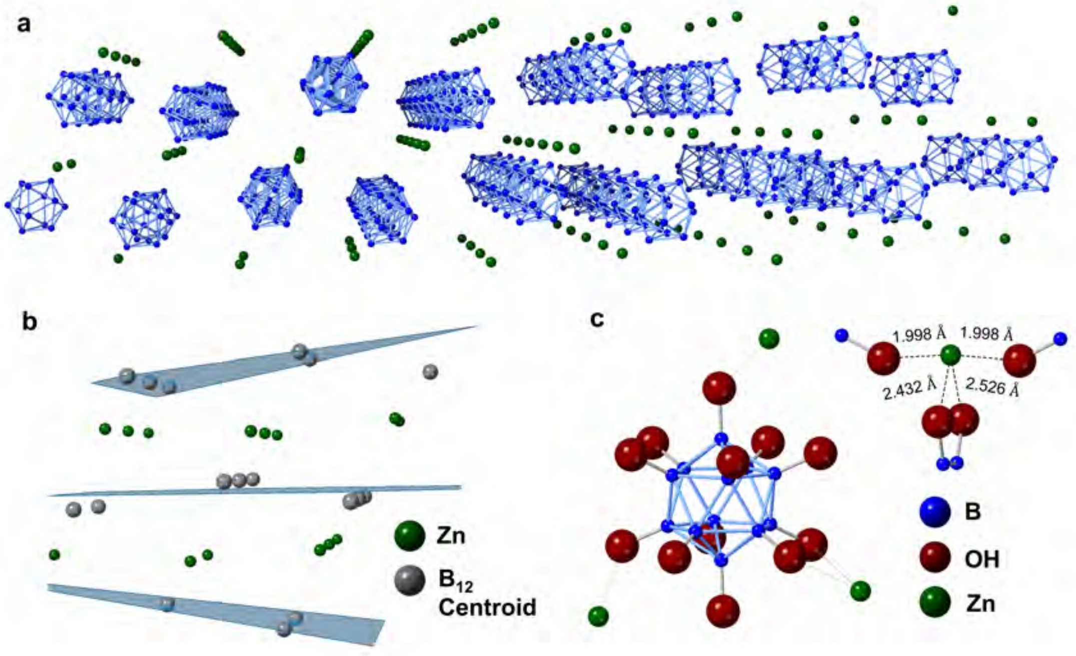

Fig. 2 (a) Perspective view of the channels of zinc ions within the $[B_{12}(OH)_{12}]^{2-}$ framework; (-OH groups omitted for clarity). (b) 2D structure of the material, formed by alternating planes of boron clusters and Zn(II) ions, in which each boron cluster is depicted by a simplified centroid. (c) Coordination environment around a single $[B_{12}(OH)_{12}]^{2-}$ cluster (left), and around a single Zn(II) ion (right); (solvent molecules omitted for clarity).

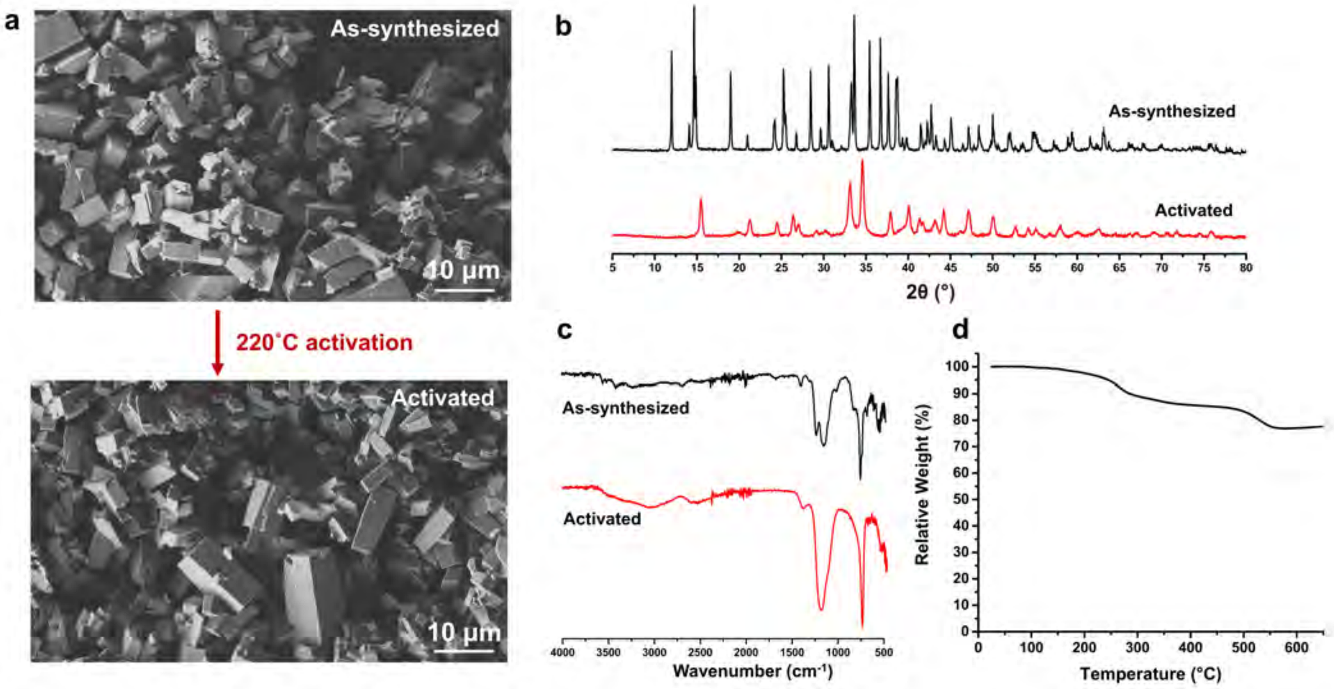

Fig. 3 (a) SEM images of $ZnB_{12}(OH)_{12}$ as-synthesized (top) and after activation (bottom) at 220°C under vacuum. (b) PXRD patterns before (black) and after (red) activation. (c) FTIR of as-synthesized (black) and activated (red) material (d) TGA of as-synthesized $ZnB_{12}(OH)_{12}$.

Synthesis

$ZnB_{12}(OH)_{12}$ was synthesized via cation exchange of the starting material $Cs_2[B_{12}(OH)_{12}]$ (Fig. 1a) by leveraging the effect that the counterion of the boron cluster has on the solubility of the material. The cesium-coordinated cluster is soluble in hot aqueous solution, while the final zinc-coordinated cluster is insoluble in water. The material was recovered after centrifugation and subjected to lyophilization. The resulting solid white powder still contains water molecules in the crystal lattice, as evident by various characterization methods (see below).

XRD Characterization

As discussed in the experimental section, XRD refinement was particularly useful in elucidating the structural features of this material (Fig. 2). Structure determination was aided by the use of TOPAS, which allowed the identification of a monoclinic *C*2/*m* space group. Density measurements of the powder in a pycnometer confirmed that the experimental density of 2.27 g/cm^3 was in good agreement with the predicted density of 2.30 g/cm^3. From these refinement methods, we determined the structure consists of six-coordinate Zn(II) ions, coordinating to three boron clusters by four bonding interactions (Fig. 2c) and two solvent molecules. Each Zn(II) ion is chemically equivalent, and is bound in a bidentate fashion by two -OH groups on one cluster, with bond lengths of 2.432 Å and 2.526 Å, and bound in a monodentate fashion by hydroxyl moieties on two additional clusters, with equivalent bond lengths of 1.998 Å. The coordination environment around each Zn(II) ion is completed with two coordinating H_2O molecules, in good agreement with the preference of Zn(II) for a six-coordinate environment in aqueous solution[64-66]. However, the mass loss observed by TGA upon thermal activation more closely agrees with three H_2O molecules per $ZnB_{12}(OH)_{12}$ unit, therefore we suspect the presence of a third unbound H_2O molecule located elsewhere in the crystal lattice. We then set out to determine if these solvent molecules can be removed, and how that would affect the material properties.

Rehydration and Solvent Exchange

In an attempt to achieve milder activation conditions, an acetone solvent exchange was attempted on an as-synthesized material. However, there were no noticeable differences in the TGA or PXRD pattern of the resulting material after it was exposed to acetone for 72 hours (Fig. S15 and S15). Additionally, we investigated whether the activated material could be rehydrated to its as-synthesized form by exposure to water/humidity. Water sorption isotherms for the activated material showed very minor adsorption (Fig. S12). Longer duration rehydration studies were then conducted to try to achieve a reversion to the PXRD pattern of the as-synthesized material. The activated material showed no change in its PXRD pattern after 8 days in a high humidity chamber (Fig. S13). Interestingly, however, full conversion back to the as-synthesized pattern was achieved for an activated sample after stirring in water for 5 days (Fig. S14).

Activation

While the effect of activation is not readily apparent by SEM, it is more noticeable by XRD, FTIR, TGA (Fig. 3), and solid-state NMR (Fig. 4 and 5). The XRD pattern of the activated material is strikingly different from that of the as-synthesized material (Fig. 3b). Clearly, the removal of coordinated solvent molecules upon thermal activation impacts the crystal structure and the long-range order. This makes additional refinements challenging but emphasizes the utility of solid-state NMR spectroscopy (see below). Despite having fewer total peaks, there appears to be a number of peaks which are retained upon activation, albeit significantly broadened and shifted, consistent with the changes in XRD patterns seen by Jorgensen et al. for various alkali metal $[B_{12}(OH)_{12}]^{2-}$ compounds upon thermal activation[16]. We hypothesize that the loss of various peaks in the low 2θ region (10-15°) could be due to a contraction of the unit cell, whereupon the removal of coordinated water molecules, proximate boron clusters move in to fill the vacant coordination sites on the Zn(II) ions. This is consistent with the solid-state NMR characterization (see below), where the proportion of hydroxyl groups coordinating the Zn(II) ions seems to increase upon thermal activation. There are also noticeable differences in the FTIR spectrum (Fig. 3c), where the two peaks at 1207 cm^{-1} and 1127 cm^{-1}, and their small shoulders, in the as-synthesized material merge into one broadened peak at 1169 cm^{-1} in the IR spectrum of the activated material. The peak at 1207 cm^{1} is assigned to a B—B stretch associated with a "breathing/pulsation" of the icosahedral cage,[21, 67-69] while the peak at 1127 cm^{-1} could be due to either a B—B cage vibration or a B—O vibrational mode. Similarly, the shouldering on either side of the peak at 726 cm^{-1} in the as-synthesized material disappears upon activation to give one peak at 718 cm^{-1}. This peak is also associated with the B—B breathing mode. Additionally, the loss of the small peaks between 3400 cm^{-1} and 3550 cm^{-1} is attributed to the removal of coordinated water upon activation. The activation of this material is further observable by TGA (Fig. 3d), which shows a mass loss of approximately 12% between 200-250°C, which we attribute to the loss of three water molecules per $ZnB_{12}(OH)_{12}$ unit. The effects of activation are most obvious, however, upon examination of the solid-state NMR spectra.

Distribution of Local Boron Environments

Solid-state NMR analyses show that the presence of Zn(II) cations influences the local environments of the hydrogen and boron atoms of the cluster, though to differing extents, according to their nanoscale proximities and interactions. This is evident in Fig. 4a, where the Hahn-echo ^{1}H MAS NMR spectrum (shown along the right vertical axis) exhibits a broad distribution of ^{1}H intensity, representing a continuous distribution of hydrogen moieties. ^{1}H signals at higher frequencies (higher chemical shifts) arise from moieties that are relatively deshielded, consistent with their nanoscale proximities to the electron-withdrawing Zn(II) ions. By comparison, ^{1}H signals at lower frequencies (lower chemical shifts) manifest more shielded environments and are expected to be more distant from the zinc cations.

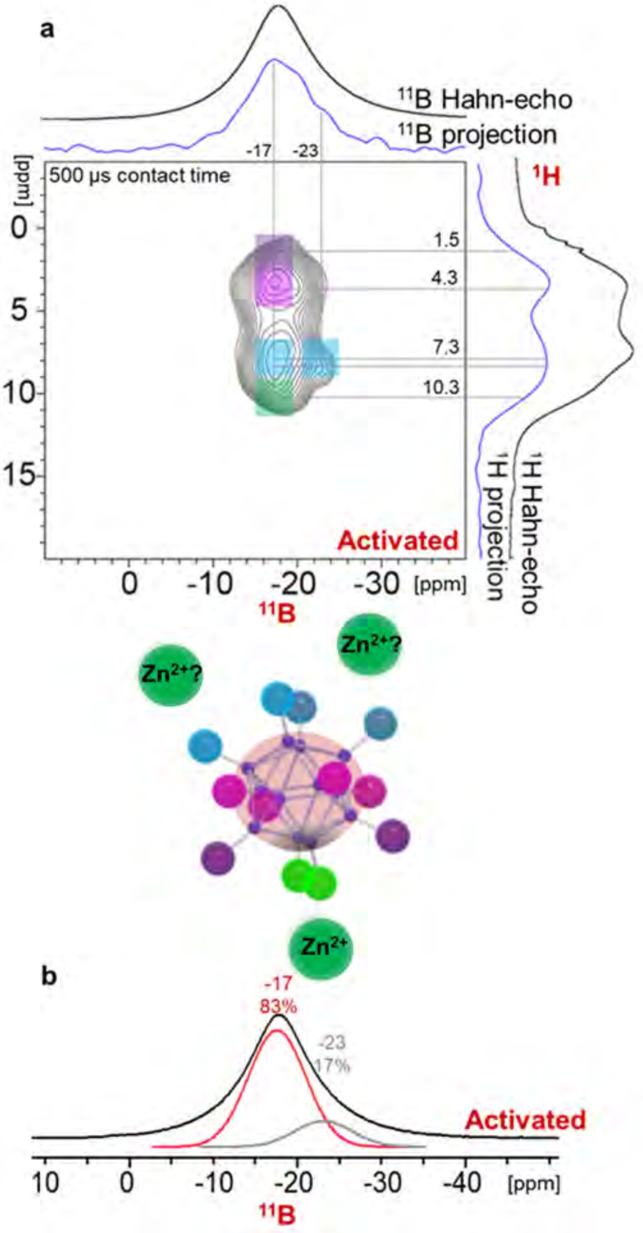

Fig. 4 (a) Solid-state 2D $^{11}B\{^{1}H\}$ HETCOR NMR spectrum of the activated Zn(II)-boron cluster material acquired at 18.8 T, 298 K, 25 kHz MAS and with a short 0.5 ms contact time. Different regions of correlated intensity are marked by colored squares that correspond to ^{1}H nuclei in different local environments that are dipole-dipole-coupled to ^{11}B nuclei in the clusters. A schematic diagram is shown of a single Zn(II)-boron cluster with hydroxylated moieties that are colored according to their local environments, consistent with the 2D spectrum. (b) 1D Hahn-echo ^{11}B MAS NMR spectrum acquired under the same conditions as (a), with two partially resolved signals that are deconvolved based on their positions and widths in the 2D spectrum, which are attributed to boron atoms on the cluster in different electronic environments, as indicated by the red or gray shading.

These different ^{1}H moieties are shown to be unambiguously associated with the Zn(II)-boron clusters by the 2D $^{11}B\{^{1}H\}$ heteronuclear correlation (HETCOR) NMR spectrum of the activated material in Fig. 4a. 2D intensity manifests pairs of correlated ^{11}B and ^{1}H nuclear spins that are in nanoscale proximity to one another. Specifically, the intensity distribution in the 2D $^{11}B\{^{1}H\}$ spectrum in Fig. 4a shows a predominant ^{11}B signal at -17 ppm, which is associated with the $[B_{12}(OH)_{12}]^{2-}$ cluster, as previously established[19]. Interestingly, for the activated material the increased resolution provided by 2D NMR reveals that there are at least two types of ^{1}H nuclei. These are characterized by isotropic chemical shifts centered at 7.3 ppm (blue) and 4.3 ppm (mauve), and are attributed to moieties that are closer to or more distant from the Zn(II) ions, respectively. Unresolved shoulders of these ^{1}H signals near 10.3 ppm (green) and 1.5 ppm (purple) indicate a broad distribution of local hydroxyl environments, which are discussed in more detail below. In addition, a distinct shoulder is notably present in the ^{11}B dimension at -23 ppm, which is correlated principally with the ^{1}H signal at 7.3 ppm (blue), consistent with these moieties being near the electron-withdrawing Zn(II) ions. The shielding of these ^{11}B nuclei is consistent with the local electron density visualized by Mulliken charges on the geometry-optimized model system (Supplementary Information; Fig. S1, S4, S7). This suggests that the well-established, delocalized, 3D-aromatic character of the boron cluster compensates for the low electron density (deshielding) of ^{1}H nuclei on the hydroxyl groups that interact most strongly with the Zn(II) ions by increasing the local electron density on proximate boron atoms. The enhanced resolution of the 2D NMR spectra enables the positions and linewidths of the two ^{11}B signals to be determined for use in deconvoluting the approximately quantitative 1D ^{11}B MAS spectrum in Fig. 4b, yielding relative integrated intensities of 83% (red) and 17% (gray) for the signals at -17 ppm and -23 ppm, respectively. This corresponds to a 5:1 ratio, which indicates a unique chemical environment for 2 boron atoms in the cluster and a separate environment for the other 10 boron atoms (red and gray shading on the cluster in Fig. 4). DFT calculations indicate that the electron densities (as visualized by Mulliken charges) on the two boron atoms whose -OH groups are involved in a bidentate Zn(II)-binding motif (Fig. 2c) are significantly higher than the other ten boron atoms on the cluster, which includes those involved in monodentate interactions and those not involved in binding interactions (Fig. S7). These two distinct chemical environments on the cluster account for the relative 1:5 ratio of boron atoms derived from integration of the 1D ^{11}B MAS NMR spectrum. Overall, however, the chemical shifts of the boron atoms in the cluster seem to be only moderately affected by the Zn(II)-hydroxyl binding interactions.

Hydroxyl Interactions at Boron Cluster Termini

Compared to boron atoms in the cluster, however, their associated hydroxyl moieties experience a much richer range of interactions with the Zn(II) cations and with each other. In particular, the spatial proximities of the different types of ^{1}H moieties can be probed by 2D $^{1}H\{^{1}H\}$ double-quantum–single-quantum (DQ-SQ) correlation NMR analyses, which resolve pairs of dipole-dipole-coupled ^{1}H nuclei according to their correlated isotropic chemical shifts. In a 2D $^{1}H\{^{1}H\}$ DQ-SQ spectrum, intensity along the double-diagonal line corresponds to dipolar-coupled ^{1}H nuclei in moieties with identical isotropic chemical shifts (and thus in the same local environments). Intensity that is displaced off the double-diagonal corresponds to coupled ^{1}H spins in different environments that are within nanoscale proximity to each other. DFT modelling of local shielding environments of the different ^{1}H moieties (Supplementary Information; Figs. S3, S6, S9) aids the assignment of the 2D-resolved signals.

For example, the 2D $^{1}H\{^{1}H\}$ DQ-SQ correlation spectrum in Fig. 5a of the as-synthesized Zn(II)-boron cluster material shows intensity maxima along the double-diagonal centered at 8 ppm (green dot), which is associated with pairs of dipole-dipole coupled hydroxyl groups that are in similar environments. The intensity maximum along the double-diagonal centered at 6 ppm (orange dot) is attributed to structural water[70].

Strong off-double-diagonal intensity is also observed at 16.5 ppm in the double-quantum dimension and at 10.5 ppm and 6 ppm (green squares) in the single-quantum dimension, consistent with the nanoscale proximity of hydroxyl groups directly engaging in a bidentate binding interaction with a Zn(II) cation, and those next-distant on the boron cluster. Similarly, strong off-double-diagonal intensity at 14.5 ppm and 10.5 ppm in the DQ dimension is correlated with pairs of ^{1}H SQ signals at 10.5 ppm and 4 ppm (blue squares), and at 8 ppm and 2.5 ppm (purple squares), respectively, each manifesting dipole-dipole-coupled ^{1}H nuclei in hydroxyl moieties which are increasingly distant from the bidentate-bound Zn(II) cations, therefore corresponding to hydroxyl groups which are either not binding with a Zn(II) ion or are engaging in a weaker monodentate bond. Additionally, strong off-diagonal intensity at 12 ppm in the DQ dimension is associated with correlated ^{1}H SQ signals centered at 8 ppm and 4 ppm (orange squares), which manifests interactions between structural water and the hydroxyl moieties of the boron cluster. It is interesting to note the absence of correlated intensity along the double-diagonal at 21 ppm in the DQ dimension and at 10.5 ppm in the SQ dimension, which establishes that these hydroxyl moieties associated with strong Zn(II) interactions are relatively isolated (>1 nm) from each other.

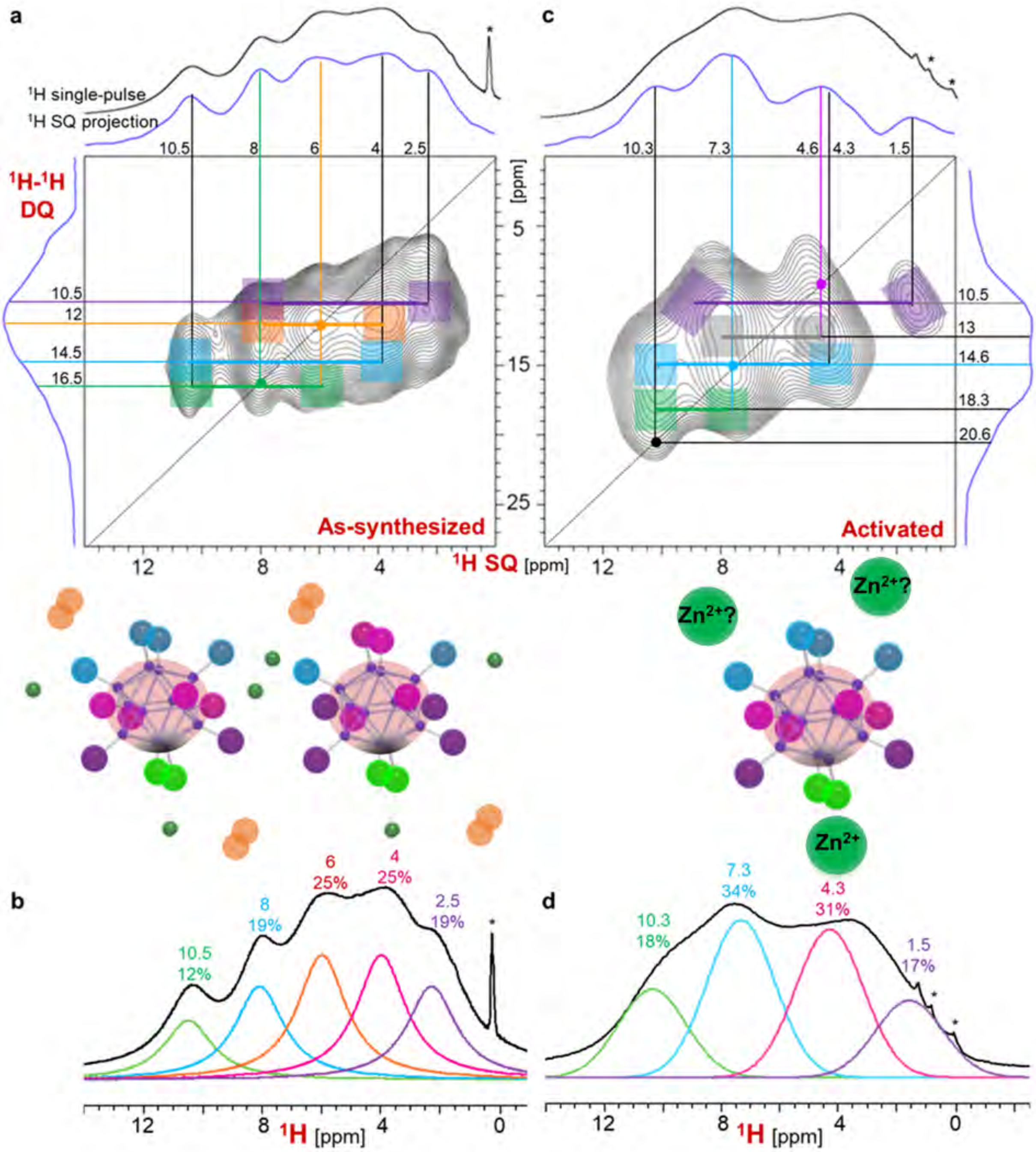

Fig 5. Solid-state (a,c) 2D $^1H\{^1H\}$ double-quantum/single-quantum correlation NMR spectra, (b,d) quantitative 1D Hahn-echo ^1H MAS NMR spectra of as-synthesized (a,b) and activated (c,d) boron cluster materials. The NMR spectra were acquired at 18.8 T, 298 K, and 25 kHz MAS. The colored regions at local intensity maxima along the dotted line highlight correlated isotropic chemical shifts arising from proximate (1 nm) dipole-dipole-coupled ^1H-^1H moieties. Signal assignments and widths in the 2D spectra were used to deconvolve and integrate the partially resolved signals in the 1D spectra in (b,d). Schematic diagrams of Zn(II)-boron clusters are shown with the Zn(II) ions (dark green), boron atoms (small, dark purple), and -OH groups colored according to their deconvoluted signal assignments. The asterisks denote impurity species.

Importantly, the improved resolution afforded by the 2D $^1H\{^1H\}$ DQ-SQ NMR analysis enables the positions and linewidths of the otherwise broad and poorly resolved signals to be deconvolved in Fig. 5b, which shows the 1D Hahn-echo ^1H MAS NMR spectrum of the as-synthesized Zn(II)-boron cluster material. Integration of the deconvoluted ^1H signals yields estimates of the relative populations of the different hydroxyl moieties (Fig. 5b), specifically 12%, 19%, 25%, and 19% for the signals at 10.5 ppm, 8 ppm, 4 ppm, and 2.5 ppm, respectively, and 25% associated with the signal at 6 ppm from structural water, the latter of which is consistent with the presence of two water molecules per boron cluster. Discounting the contribution from such structural water, the relative populations of the remaining boron-associated hydroxyl groups occur in an approximate ratio of 2:3:4:3 for the ^1H signals at 10.5 ppm, 8, 4, and 2.5 ppm, respectively, which is consistent with the expected stoichiometry of 12 hydroxyl moieties terminating each icosahedral boron cluster. This ratio appears be an average of ratios corresponding to two distinct boron cluster motifs, wherein small changes in the local chemical environment of the hydroxyl moieties (presumably due to disordered water molecules) results in distinct ratios of 2:4:4:2 and 2:2:4:4 for the respective ^1H signals. Mulliken charges visualized through DFT calculations (Fig. S9) provide estimates of the relative extent of shielding of hydrogen atoms in the hydroxyl moieties, which allows tentative assignment of the 2D-resolved isotropic chemical shifts to their local structural environments. A schematic diagram in Fig. 5b shows the two proposed structural motifs, with the colors of the different hydroxyl groups corresponding to those associated with the resolved ^1H signals in the 2D NMR spectrum of Fig. 5a.

Atomic-level Changes Produced by Thermal Activation

Upon post-synthetic activation at 220°C under vacuum, structural water molecules are lost and the $ZnB_{12}(OH)_{12}$ clusters undergo atomic-scale structural changes, which are manifested by the 2D $^1H\{^1H\}$ DQ-SQ NMR spectrum in Fig. 5c. Similar intensity maxima are observed in the activated material at 10.3 ppm, 7.3 ppm, and approximately 4.3 ppm in the SQ dimension of the 2D spectrum (blue and gray squares) as was observed for the as-synthesized material (Fig. 5a). However, there are several notable differences, including a substantial reduction in intensity of the signal at 6 ppm in the SQ dimension, which importantly manifests the loss of structural water that occurs upon thermal activation, and is corroborated separately by thermogravimetric analysis. In addition, new correlated intensity is observed at high frequency along the double-diagonal line at 20.6 ppm in the DQ dimension and at 10.3 ppm in the SQ dimension (black dot), which establishes the nanoscale proximity of these moieties that were previously isolated (Fig. 5a), consistent with densification induced by thermal treatment. Correlated intensity is furthermore observed for these high-frequency signals at 18.3 ppm in the DQ dimension with ^1H SQ signals at 10.3 ppm and approximately 8 ppm, perhaps due to the hydroxyl groups having closer proximities to or enhanced binding with the Zn(II) cations after activation. Finally, a large change is also observed in the low-frequency ^1H signals, which exhibit a well resolved ^1H SQ signal at 1.5 ppm that is correlated to a broad distribution of intensity at approximately 9 ppm (purple rectangles, 10.5 ppm DQ). Collectively, these results manifest in high detail the atomic-scale rearrangements that occur as a result of thermal activation.

Using the positions and linewidths established by the 2D $^1H\{^1H\}$ NMR spectrum in Fig. 5c allows for confident deconvolution of the 1D Hahn-echo ^1H MAS NMR spectrum in Fig. 5d. Integration of the deconvoluted ^1H signals yields estimates of the relative populations of the different hydroxyl moieties. The ^1H signals at 10.3 ppm, 7.3 ppm, 4.3 ppm, and 1.5 ppm account for approximately 18%, 34%, 31%, and 17% of the hydrogen atom environments, respectively. Based on these relative integrated ^1H signal intensities, the different hydroxyl moieties are established to be present in ratios of 2:4:4:2, once again consistent with the expected stoichiometry of the 12 hydroxyl moieties per boron cluster. Importantly, there is a general increase in the integrated intensities of the ^1H signals that are displaced to higher frequency; for example, ^1H signals with a chemical shift greater than or equal to 7.3 ppm have relative intensities that roughly increase from 42% to 50% upon activation of the boron cluster material. Comparison of the as-synthesized and activated spectra suggests this is because the -OH moieties on the cluster can act as hemilabile ligands, increasing their denticity upon thermal activation by switching from a monodentate Zn(II)-binding motif to a bidentate interaction. In doing so, the open coordination sites on the metal ion which are exposed after removal of coordinated water molecules are filled by -OH groups from the cluster. This is reflected by an increase in relative intensities of the ^1H signals that represent hydrogens in more deshielded environments. The schematic diagram in Fig. 5d for the activated material shows a hydroxyl-terminated boron cluster near intercalated Zn(II) ions, with the colors of the different hydroxyl H atoms corresponding to those associated with the resolved ^1H signals in Fig. 5c, and relative populations that are consistent with the ^1H ratios established by Fig. 5d. Because there was no crystallographic refinement performed on the activated material, the locations of the Zn(II) ions are tentatively proposed in this schematic (large green circles, Fig. 5d), although it is expected that the proportion of bidentate-bound Zn(II) ions is higher. Thus, the enhanced signal resolution and atomic-scale insights provided by the 1D and 2D solid-state NMR analysis yield detailed information about the dynamic interactions between the Zn(II) cations and the hydroxylated boron cluster, along with atomic-scale differences between the as-synthesized and activated cluster materials.

Conclusions

A divalent Zn(II) dodecahydroxy-*closo*-dodecaborate coordination polymer was synthesized and thoroughly characterized via a variety of spectroscopic and structural methods. The removal of solvent molecules from the crystal lattice of the as-synthesized material was rigorously studied, providing key atomic insights into the changes in chemical environment of the perhydroxylated boron cluster ligand. Increased atomic level understandings were elucidated from solid state 1D and 2D NMR analyses of the as-synthesized and activated materials. Subtle changes in the electronic environment of both the boron atoms comprising the cluster and the -OH moieties on the cluster were investigated. The location of Zn(II) ions and their binding modes (monodentate or bidentate) were revealed to have moderate effects on the relative shielding of ^{11}B nuclei and significant effects on the shielding of ^1H nuclei, as evident by thorough analyses of the solid-state NMR spectra. Furthermore, 2D $^1H\{^1H\}$ double-quantum/single-quantum correlation NMR spectra were correlated with quantitative 1D Hahn-echo ^{1}H MAS NMR spectra, suggesting that $[B_{12}(OH)_{12}]^{2-}$ contains hemilabile -OH moieties, which can switch from monodentate to bidentate interactions with Zn(II) ions to fill vacant coordination sites generated on the metal ion upon the removal of coordinated water molecules. This is the first observation of the complex behavior of a $[B_{12}(OH)_{12}]^{2-}$ anion acting as a multidentate ligand with a transition metal ion. This analysis represents a valuable contribution to the field of coordination polymers, in which solid-state NMR is becoming recognized as a powerful tool for the elucidation of atomic-level structures.[71-80] Overall, the increased multi-scale characterizations and understandings provided here for the first time in these types of materials will pave the way for further studies into coordination polymers, especially those composed of boron cluster building blocks.

Conflicts of interest

There are no conflicts to declare.

Acknowledgements

This work was supported as part of the Center for Synthetic Control Across Length scales for Advancing Rechargeables (SCALAR), an Energy Frontier Research Center funded by the U.S. Department of Energy, Office of Science, Basic Energy Sciences under Award DE-SC0019381. The research reported here made use of shared facilities of the UC Santa Barbara Materials Research Science and Engineering Center (MRSEC, NSF DMR 1720256), a member of the Materials Research Facilities Network (www.mrfn.org). We would like to thank Karam B. Idrees and Prof. Omar K. Farha (Northwestern University) for aid in performing the adsorption experiments.

Notes and references

1. S. R. Batten, S. M. Neville and D. R. Turner, *Coordination Polymers: Design, Analysis and Application*, 2008.
2. A.-C. Stoica, M. Damoc, M.-F. Zaltariov, C. Racles and M. Cazacu, *React. Funct. Polym.*, 2021, **168**, 105039.
3. E. Fernandez-Bartolome, A. Martinez-Martinez, E. Resines-Urien, L. Piñeiro-Lopez and J. S. Costa, *Coordination Chemistry Reviews*, 2022, **452**, 214281.
4. A. M. Spokoyny, *Pure and Applied Chemistry*, 2013, **85**, 903.
5. M. F. Hawthorne and A. Pushechnikov, *Pure and Applied Chemistry*, 2012, **84**, 2279-2288.
6. B. P. Dash, R. Satapathy, J. A. Maguire and N. S. Hosmane, *New Journal of Chemistry*, 2011, **35**, 1955-1972.
7. B. R. S. Hansen, M. Paskevicius, H.-W. Li, E. Akiba and T. R. Jensen, *Coordination Chemistry Reviews*, 2016, **323**, 60-70.
8. F. Cheng and F. Jäkle, *Polymer Chemistry*, 2011, **2**, 2122-2132.
9. R. Núñez, I. Romero, F. Teixidor and C. Viñas, *Chemical Society Reviews*, 2016, **45**, 5147-5173.
10. A. N. Alexandrova, A. I. Boldyrev, H.-J. Zhai and L.-S. Wang, *Coordination Chemistry Reviews*, 2006, **250**, 2811-2866.
11. N. Das, P. J. Stang, A. M. Arif and C. F. Campana, *The Journal of Organic Chemistry*, 2005, **70**, 10440-10446.
12. O. K. Farha, A. M. Spokoyny, K. L. Mulfort, S. Galli, J. T. Hupp and C. A. Mirkin, *Small*, 2009, **5**, 1727-1731.
13. O. K. Farha, A. M. Spokoyny, K. L. Mulfort, M. F. Hawthorne, C. A. Mirkin and J. T. Hupp, *Journal of the American Chemical Society*, 2007, **129**, 12680-12681.
14. L. Gan, A. Chidambaram, P. G. Fonquernie, M. E. Light, D. Choquesillo-Lazarte, H. Huang, E. Solano, J. Fraile, C. Viñas, F. Teixidor, J. A. R. Navarro, K. C. Stylianou and J. G. Planas, *Journal of the American Chemical Society*, 2020, **142**, 8299-8311.
15. L. Gan, P. G. Fonquernie, M. E. Light, G. Norjmaa, G. Ujaque, D. Choquesillo-Lazarte, J. Fraile, F. Teixidor, C. Viñas and J. G. Planas, *Molecules*, 2019, **24**.
16. M. Jørgensen, S. R. H. Jensen, T. D. Humphries, M. R. Rowles, M. V. Sofianos, C. E. Buckley, T. R. Jensen and M. Paskevicius, *The Journal of Physical Chemistry C*, 2020, **124**, 11340-11349.
17. H. Jude, H. Disteldorf, S. Fischer, T. Wedge, A. M. Hawkridge, A. M. Arif, M. F. Hawthorne, D. C. Muddiman and P. J. Stang, *Journal of the American Chemical Society*, 2005, **127**, 12131-12139.
18. D. Jung, M. Muni, G. Marin, R. Ramachandran, M. F. El-Kady, T. Balandin, R. B. Kaner and A. M. Spokoyny, *Journal of Materials Chemistry A*, 2020, **8**, 18015-18023.
19. D. Jung, L. M. A. Saleh, Z. J. Berkson, M. F. El-Kady, J. Y. Hwang, N. Mohamed, A. I. Wixtrom, E. Titarenko, Y. Shao, K. McCarthy, J. Guo, I. B. Martini, S. Kraemer, E. C. Wegener, P. Saint-Cricq, B. Ruehle, R. R. Langeslay, M. Delferro, J. L. Brosmer, C. H. Hendon, M. Gallagher-Jones, J. Rodriguez, K. W. Chapman, J. T. Miller, X. Duan, R. B. Kaner, J. I. Zink, B. F. Chmelka and A. M. Spokoyny, *Nature Materials*, 2018, **17**, 341-348.
20. D. Nguyen, Institut für Anorganische Chemie der Universität Stuttgart, 2009.
21. T. Peymann, C. B. Knobler and M. F. Hawthorne, *Inorg. Chem.*, 2000, **39**, 1163-1170.
22. T. Peymann, C. B. Knobler, S. I. Khan and M. F. Hawthorne, *Journal of the American Chemical Society*, 2001, **123**, 2182-2185.
23. S. Rodríguez-Hermida, M. Y. Tsang, C. Vignatti, K. C. Stylianou, V. Guillerm, J. Pérez-Carvajal, F. Teixidor, C. Viñas, D. Choquesillo-Lazarte, C. Verdugo-Escamilla, I. Peral, J. Juanhuix, A. Verdaguer, I. Imaz, D. Maspoch and J. Giner Planas, *Angewandte Chemie International Edition*, 2016, **55**, 16049-16053.
24. T. Scholköpf, Institut für Anorganische Chemie der Universität Stuttgart, 2011.
25. A. M. Spokoyny, D. Kim, A. Sumrein and C. A. Mirkin, *Chemical Society Reviews*, 2009, **38**, 1218-1227.
26. F. Tan, A. López-Periago, M. E. Light, J. Cirera, E. Ruiz, A. Borrás, F. Teixidor, C. Viñas, C. Domingo and J. G. Planas, *Advanced Materials*, 2018, **30**, 1800726.

27. M. Y. Tsang, S. Rodríguez-Hermida, K. C. Stylianou, F. Tan, D. Negi, F. Teixidor, C. Viñas, D. Choquesillo-Lazarte, C. Verdugo-Escamilla, M. Guerrero, J. Sort, J. Juanhuix, D. Maspoch and J. Giner Planas, *Crystal Growth & Design*, 2017, **17**, 846-857.
28. N. Van, I. Tiritiris, R. F. Winter, B. Sarkar, P. Singh, C. Duboc, A. Muñoz-Castro, R. Arratia-Pérez, W. Kaim and T. Schleid, *Chemistry – A European Journal*, 2010, **16**, 11242-11245.
29. T. J. Wedge, A. Herzog, R. Huertas, M. W. Lee, C. B. Knobler and M. F. Hawthorne, *Organometallics*, 2004, **23**, 482-489.
30. Y. Zhang, L. Yang, L. Wang, S. Duttwyler and H. Xing, *Angewandte Chemie International Edition*, 2019, **58**, 8145-8150.
31. Z. Zheng, C. B. Knobler, M. D. Mortimer, G. Kong and M. F. Hawthorne, *Inorg. Chem.*, 1996, **35**, 1235-1243.
32. A. R. Pitochelli and F. M. Hawthorne, *Journal of the American Chemical Society*, 1960, **82**, 3228-3229.
33. I. Sivaev, V. Bregadze and S. Sjöberg, *Collection of Czechoslovak Chemical Communications*, 2002, **67**.
34. E. L. Muetterties, J. H. Balthis, Y. T. Chia, W. H. Knoth and H. C. Miller, *Inorg. Chem.*, 1964, **3**, 444-451.
35. W. H. Knoth, H. C. Miller, J. C. Sauer, J. H. Balthis, Y. T. Chia and E. L. Muetterties, *Inorg. Chem.*, 1964, **3**, 159-167.
36. K. A. Solntsev, A. M. Mebel, N. A. Votinova, N. T. Kuznetsov and O. P. Charkin, *Koordinatsionnaya Khimiya*, 1992, **18**, 340-364.
37. S. V. Ivanov, S. M. Miller, O. P. Anderson, K. A. Solntsev and S. H. Strauss, *Journal of the American Chemical Society*, 2003, **125**, 4694-4695.
38. C. Knapp and C. Schulz, *Chemical Communications*, 2009, DOI: 10.1039/B908970E, 4991-4993.
39. V. Geis, K. Guttsche, C. Knapp, H. Scherer and R. Uzun, *Dalton Transactions*, 2009, DOI: 10.1039/B821030F, 2687-2694.
40. E. Bukovsky, S. Fiedler, D. V. Peryshkov, A. A. Popov and S. Strauss, *European Journal of Inorganic Chemistry*, 2012, **2012**, 208-212.
41. D. V. Peryshkov, A. A. Popov and S. H. Strauss, *Journal of the American Chemical Society*, 2010, **132**, 13902-13913.
42. D. V. Peryshkov, E. V. Bukovsky, M. R. Lacroix, H. Wu, W. Zhou, W. M. Jones, M. Lozinšek, T. C. Folsom, D. L. Heyliger, T. J. Udovic and S. H. Strauss, *Inorg. Chem.*, 2017, **56**, 12023-12041.
43. I. Krossing and I. Raabe, *Angewandte Chemie International Edition*, 2004, **43**, 2066-2090.
44. C. Jenne, M. Keßler and J. Warneke, *Chemistry – A European Journal*, 2015, **21**, 5887-5891.
45. D. V. Peryshkov and S. Strauss, *Journal of Fluorine Chemistry*, 2010, **131**, 1252-1256.
46. D. V. Peryshkov, E. V. Bukovsky, T. C. Folsom and S. H. Strauss, *Polyhedron*, 2013, **58**, 197-205.
47. M. Malischewski, D. V. Peryshkov, E. V. Bukovsky, K. Seppelt and S. H. Strauss, *Inorg. Chem.*, 2016, **55**, 12254-12262.
48. B. R. S. Hansen, M. Paskevicius, M. Jørgensen and T. R. Jensen, *Chemistry of Materials*, 2017, **29**, 3423-3430.
49. E. V. Bukovsky, D. V. Peryshkov, H. Wu, W. Zhou, W. S. Tang, W. M. Jones, V. Stavila, T. J. Udovic and S. H. Strauss, *Inorg. Chem.*, 2017, **56**, 4369-4379.
50. M. Kirchmann and L. Wesemann, *Dalton Transactions*, 2008, DOI: 10.1039/B715305H, 444-446.
51. E. A. Malinina, V. V. Avdeeva, L. V. Goeva and N. T. Kuznetsov, *Russian Journal of Inorganic Chemistry*, 2010, **55**, 2148-2202.
52. Y. Zhang, Y. Sun, F. Lin, J. Liu and S. Duttwyler, *Angewandte Chemie International Edition*, 2016, **55**, 15609-15614.
53. Y. Zhang, T. Wang, L. Wang, Y. Sun, F. Lin, J. Liu and S. Duttwyler, *Chemistry – A European Journal*, 2018, **24**, 15812-15817.
54. T. Peymann, A. Herzog, C. B. Knobler and M. F. Hawthorne, *Angewandte Chemie International Edition*, 1999, **38**, 1061-1064.
55. S. E. Korolenko, V. V. Avdeeva, E. A. Malinina and N. T. Kuznetsov, *Russian Journal of Inorganic Chemistry*, 2021, **66**, 1350-1373.
56. S. J. R. Prabakar, K. J. Rao and C. N. R. Rao, *Proceedings of the Royal Society of London. A. Mathematical and Physical Sciences*, 1990, **429**, 1 - 15.
57. K. R. Thurber and R. Tycko, *Journal of magnetic resonance (San Diego, Calif. : 1997)*, 2009, **196**, 84-87.
58. J. P. Yesinowski, H. D. Ladouceur, A. P. Purdy and J. B. Miller, *J. Chem. Phys.*, 2010, **133**, 234509.
59. M. Weingarth and M. Baldus, in *Illustrated Medical Biochemistry*, Jaypee Brothers Medical Publishers Ltd., 2005, ch. 1.
60. M. H. Levitt, *Spin Dynamics: Basics of Nuclear Magnetic Resonance*, John Wiley & Sons, 2 edn., 2008.
61. I. Schnell and H. W. Spiess, *J Magn Reson*, 2001, **151**, 153-227.
62. M. Feike, D. E. Demco, R. Graf, J. Gottwald, S. Hafner and H. W. Spiess, *Journal of Magnetic Resonance, Series A*, 1996, **122**, 214-221.
63. K. Saalwächter, F. Lange, K. Matyjaszewski, C. F. Huang and R. Graf, *J Magn Reson*, 2011, **212**, 204-215.
64. M. Dudev, J. Wang, T. Dudev and C. Lim, *The Journal of Physical Chemistry B*, 2006, **110**, 1889-1895.
65. Y. Marcus, *Chemical Reviews*, 1988, **88**, 1475-1498.
66. H. Ohtaki and T. Radnai, *Chemical Reviews*, 1993, **93**, 1157-1204.
67. T. Peymann, C. B. Knobler, S. I. Khan and M. F. Hawthorne, *Inorg. Chem.*, 2001, **40**, 1291-1294.
68. E. L. Muetterties, R. E. Merrifield, H. C. Miller, W. H. Knoth, Jr. and J. R. Downing, *J Am Chem Soc*, 1962, **84**, 2506.
69. L. A. Leites, *Chemical Reviews*, 1992, **92**, 279-323.
70. B. Grünberg, T. Emmler, E. Gedat, I. Shenderovich, G. H. Findenegg, H. H. Limbach and G. Buntkowsky, *Chemistry*, 2004, **10**, 5689-5696.
71. P. M. Aguiar, M. J. Katz, D. B. Leznoff and S. Kroeker, *Physical Chemistry Chemical Physics*, 2009, **11**, 6925-6934.
72. H. A. Habib, A. Hoffmann, H. A. Höppe and C. Janiak, *Dalton Transactions*, 2009, DOI: 10.1039/B812670D, 1742-1751.
73. H. A. Habib, A. Hoffmann, H. A. Höppe, G. Steinfeld and C. Janiak, *Inorg. Chem.*, 2009, **48**, 2166-2180.
74. S. D. Jones, H. Nguyen, P. M. Richardson, Y.-Q. Chen, K. E. Wyckoff, C. J. Hawker, R. J. Clément, G. H. Fredrickson and R. A. Segalman, *ACS Central Science*, 2022, DOI: 10.1021/acscentsci.1c01260.

75. M. J. Katz, P. M. Aguiar, R. J. Batchelor, A. A. Bokov, Z.-G. Ye, S. Kroeker and D. B. Leznoff, *Journal of the American Chemical Society*, 2006, **128**, 3669-3676.
76. A. V. Kuttatheyil, D. Lässig, J. Lincke, M. Kobalz, M. Baias, K. König, J. Hofmann, H. Krautscheid, C. J. Pickard, J. Haase and M. Bertmer, *Inorg. Chem.*, 2013, **52**, 4431-4442.
77. H. H. Lee, J. B. Lee, Y. Park, K. H. Park, M. S. Okyay, D.-S. Shin, S. Kim, J. Park, N. Park, B.-K. An, Y. S. Jung, H.-W. Lee, K. T. Lee and S. Y. Hong, *ACS Applied Materials & Interfaces*, 2018, **10**, 22110-22118.
78. L. Ouyang, P. M. Aguiar, R. J. Batchelor, S. Kroeker and D. B. Leznoff, *Chemical Communications*, 2006, DOI: 10.1039/B512430A, 744-746.
79. L. Rodríguez-Cid, E. C. Sañudo, A. M. López-Periago, A. González-Campo, N. Aliaga-Alcalde and C. Domingo, *Crystal Growth & Design*, 2020, **20**, 6555-6564.
80. J. J. Vittal, *Coordination Chemistry Reviews*, 2007, **251**, 1781-1795.

Electronic Supplementary Material (ESI) for Dalton Transactions.

Supplementary Information

Synthesis and structural properties of a 2D Zn(II) dodecahydroxy-*closo*-dodecaborate coordination polymer

Austin D. Ready†[a], Shona M. Becwar†[e], Dahee Jung[a,b], Anna Kallistova[c], Emily Schueller[c], Kierstyn P. Anderson[a,b], Rebecca Kubena[a], Ram Seshadri[c,d], Bradley F. Chmelka*[e], Alexander M. Spokoyny*[a,b]

†These authors contributed equally

*bradc@ucsb.edu

*spokoyny@chem.ucla.edu

[a]*Department of Chemistry and Biochemistry, University of California, Los Angeles, Los Angeles, CA, USA.*

[b]*California NanoSystems Institute (CNSI), University of California, Los Angeles, Los Angeles, CA, USA*

[c]*Materials Department and Materials Research Laboratory, University of California, Santa Barbara, Santa Barbara, CA, USA*

[d]*Department of Chemistry and Biochemistry, University of California, Santa Barbara, Santa Barbara, CA, USA*

[e]*Department of Chemical Engineering, University of California, Santa Barbara, Santa Barbara, CA, USA*

Density Functional Theory Calculations

Calculations were performed using SCM ADF software. XYZ coordinates for $[B_{12}(OH)_{12}]^{2-}$ determined by refinement of the powder pattern were imported, and the structure was subsequently modified within the software to create a monodentate, bidentate, and fully bound cluster (two monodentate and one bidentate). To reduce the computational complexity, Zn(II) ions were replaced by electron-withdrawing $-CF_3$ or $-CF_2$ groups for the monodentate and bidentate interactions, respectively. Geometry pre-optimizations were performed, followed by full geometry optimizations at the GGA:PBE-D3(BJ) theory level with a DZP basis set and scalar relativistic effects considered. Electron densities were approximated by visualizing the Mulliken charges from the optimized geometries.

DFT Geometry Coordinates

Monodentate Model

B	10.03641626	0.70477989	4.25036940
B	9.86041612	0.91832069	1.37492897
B	10.84443567	1.33883616	2.78722167
B	9.07410742	1.39416003	2.90217249
B	11.31314064	-0.04102169	1.77195483
B	8.54657298	-0.09218594	3.70593632
B	8.42750664	0.04862699	1.92450214
B	11.41759731	-0.17551100	3.52625271
O	10.21046734	1.28710518	5.57590467
O	9.99484615	1.89312023	0.28857152
O	11.48592717	2.65127162	2.72393846
O	8.48212971	2.73171711	2.97793617
O	12.36948369	-0.03293479	0.76586790
O	7.28673613	-0.25303660	4.42409684

O	7.06594926	0.01815626	1.40161372
H	11.22138264	-3.03849040	1.42303935
B	9.97828320	-1.08937531	4.11664441
B	10.78877609	-1.56982927	2.59658628
B	8.99458501	-1.47693594	2.67298394
O	9.99988404	-1.85179240	5.34778269
B	9.81877147	-0.86904833	1.24406481
O	11.49367255	-2.80285841	2.33816524
O	8.02003400	-2.56062674	2.64587197
O	9.93512675	-1.58607964	-0.02013589
H	10.80854249	-1.28004740	-0.36118097
H	6.85130685	-0.94406827	1.42243947
H	8.34409045	2.98684693	2.04042765
H	10.58658644	2.57268760	0.69629076
H	10.77948059	3.25148754	3.05999258
H	11.17900886	1.31654313	5.72463849
H	12.15587060	0.74865946	0.20958506
H	9.90880745	-1.17696623	6.05535366
H	7.50484123	-2.41734468	3.47324682
H	6.61891362	0.03994560	3.76280987
O	12.61098248	-0.22071594	4.43161112
F	14.17446441	1.06937723	3.41185957
C	13.84397960	-0.12734681	4.02309306
F	14.69883623	-0.22062261	5.12404294
F	14.25598674	-1.11026051	3.15308815

Bidentate Model

B	10.08719002	0.83793251	4.15365152
B	10.18662900	0.79277030	1.28647311
B	11.11471683	1.21897185	2.73540103
B	9.35549107	1.45676299	2.65381487
B	11.50970186	-0.24497295	1.82647977
B	8.55528105	0.14078610	3.51174597
B	8.60383452	0.10338866	1.72206769
B	11.43804108	-0.25566632	3.63989979
O	10.23660844	1.51496346	5.42453822
O	10.09559733	1.92362691	0.30471646
O	12.10555178	2.28715480	2.72355915
O	8.94010744	2.79169955	2.10445065
O	12.75523581	-0.36703017	1.08153225
O	7.31536502	0.08890406	4.27346873
O	7.42048922	0.34954394	0.92752469
H	10.93590742	-3.29790186	1.74685850
B	9.86503450	-0.93063877	4.08601227
B	10.74907619	-1.60839435	2.67368650
B	8.96720243	-1.36559770	2.60135901
O	9.54118560	-1.71819790	5.26905963
B	9.97678742	-0.95042308	1.18308019
O	11.26956112	-2.96080580	2.60766596
O	8.05001624	-2.48683434	2.75053682
O	10.05367393	-1.77959689	-0.01232610
H	10.93785569	-1.58173621	-0.38816698

H	7.38928567	1.30880236	0.73402787
C	9.48363918	2.97139570	0.88358002
F	8.50142775	3.49698087	0.00698543
H	11.71540497	3.06394657	2.27038897
H	11.07810032	1.15089475	5.78003634
H	13.08809235	0.55388509	1.01592287
H	8.72380334	-1.28382750	5.60657253
H	8.34924905	-2.90421935	3.59168397
H	6.84084819	-0.67665694	3.87673939
O	12.60710806	-0.29535529	4.51024218
F	10.41364934	4.08817725	0.94332260
H	13.20874009	0.39807322	4.16827063

Full Structure Model

B	10.15980135	0.84130150	4.23769295
B	10.02051420	0.96177166	1.39389812
B	11.09379991	1.34778550	2.77642402
B	9.32285272	1.51991925	2.84546883
B	11.39727113	-0.07891761	1.75123265
B	8.57656421	0.16948167	3.70524412
B	8.48861840	0.22324826	1.92577006
B	11.46372227	-0.19458711	3.54593532
O	10.25373992	1.39206930	5.57515991
O	9.82711525	2.13613075	0.49298370
O	11.98521916	2.47772394	2.70761641
O	8.85930751	2.88354963	2.45171684

O	12.52307139	-0.22589488	0.85944380
O	7.43984764	0.32955100	4.58030387
O	7.22327202	0.48467757	1.28776126
H	10.90561051	-3.12990936	1.56014048
B	9.93666727	-0.94077548	4.14293646
B	10.71783061	-1.51370271	2.61583974
B	8.93099182	-1.29149142	2.71858643
O	9.93328829	-1.65944814	5.38522198
B	9.82085626	-0.78161505	1.23633201
O	11.27148747	-2.82295234	2.41870835
O	8.11512355	-2.52503344	2.57006013
O	9.79530136	-1.55935952	0.01373016
H	10.66121397	-1.37890537	-0.41222802
H	7.28175476	1.34217488	0.81799614
F	6.58266741	-4.07187360	2.85392118
F	7.96495809	3.42957580	0.43942726
H	11.47861182	3.25233489	2.38781232
H	9.32424349	1.46022163	5.88310144
H	13.00652706	0.62617694	0.88444732
H	10.22247482	-1.00578547	6.05925699
F	7.20326518	-2.89574551	4.61158577
H	6.66707091	0.48512425	3.99753694
O	12.65141053	-0.38385628	4.41675496
F	14.42058207	0.46030100	3.27293347
C	13.87348685	-0.57770580	4.01600546
F	14.70393867	-0.70407129	5.12504894
F	14.08342540	-1.71269257	3.26686175

C	7.04537611	-2.82069411	3.24799400
F	5.96954203	-1.96116088	3.05063756
C	9.16332276	3.10734403	1.15474564
F	9.88479304	4.33011229	1.04765589

Monodentate Model

Fig. S1 Mulliken charges on boron atoms for monodentate model

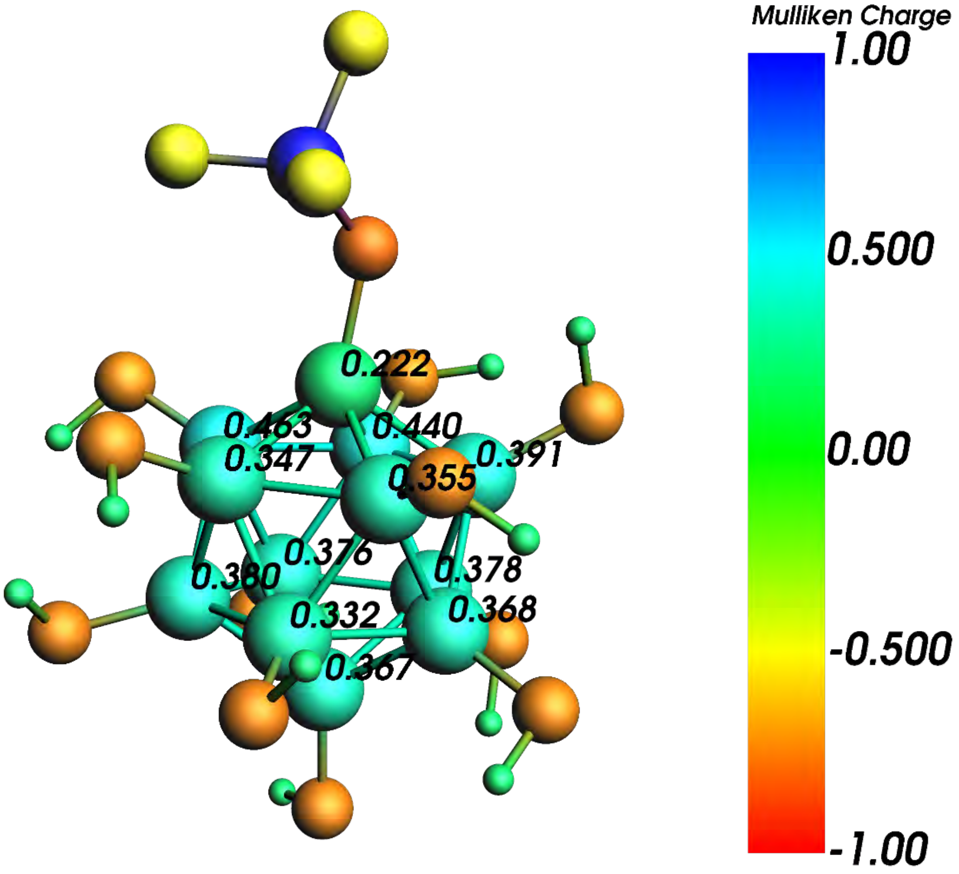

Fig. S2 Mulliken charges on oxygen atoms for monodentate model

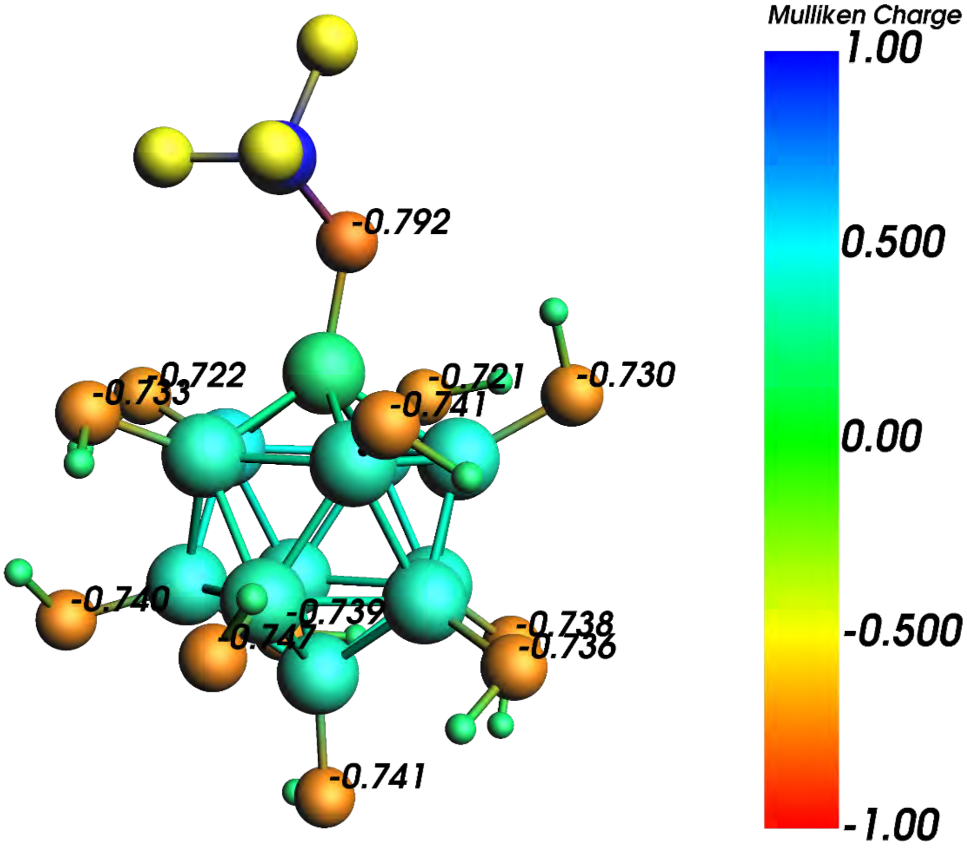

Fig. S3 Mulliken charges on hydrogen atoms for monodentate model

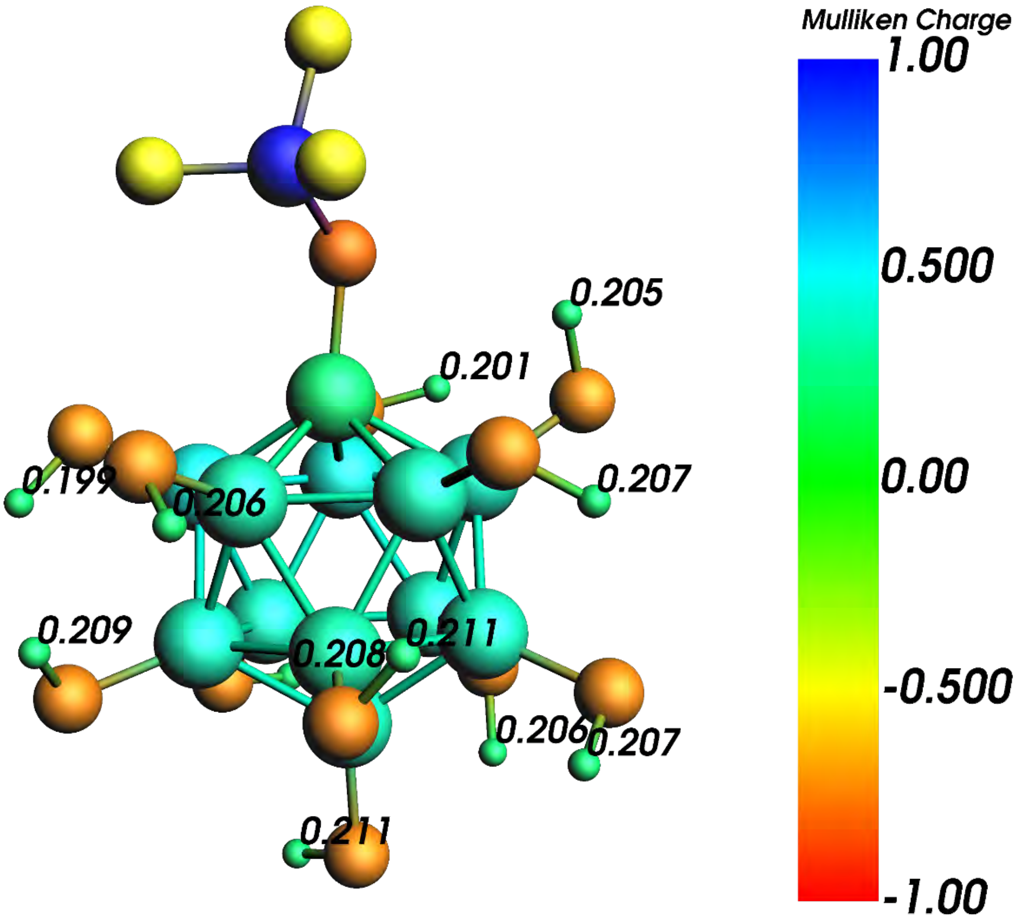

Bidentate Model

Fig. S4 Mulliken charges on boron atoms for bidentate model

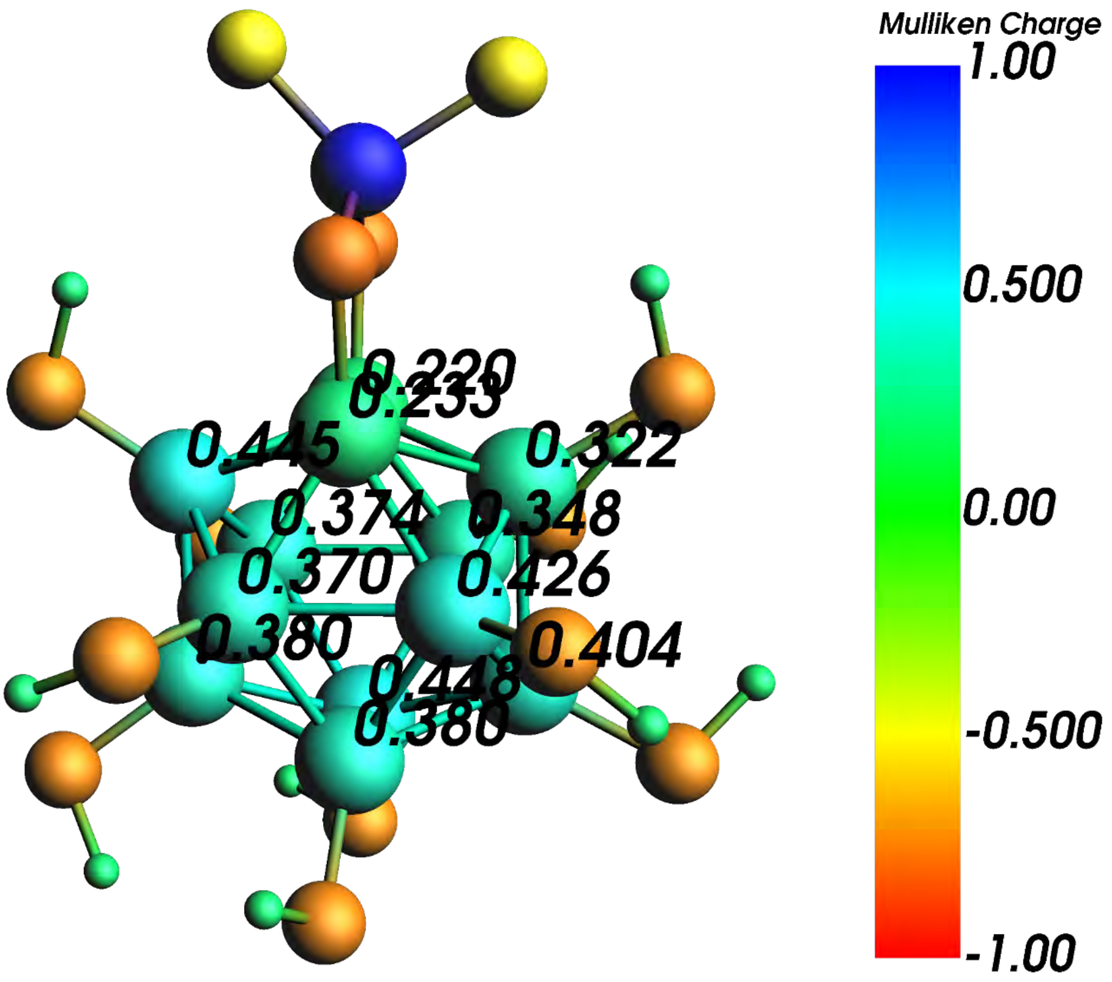

Fig. S5 Mulliken charges on oxygen atoms for bidentate model

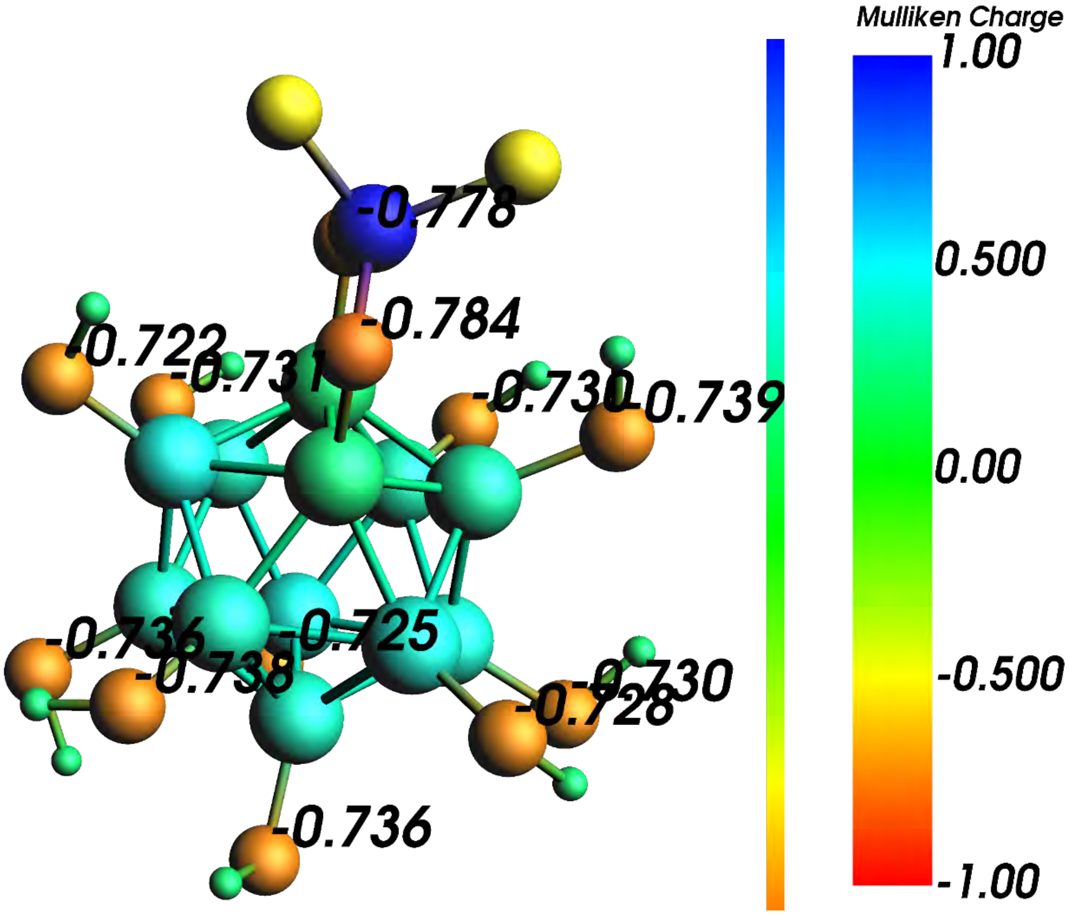

Fig. S6 Mulliken charges on hydrogen atoms for bidentate model

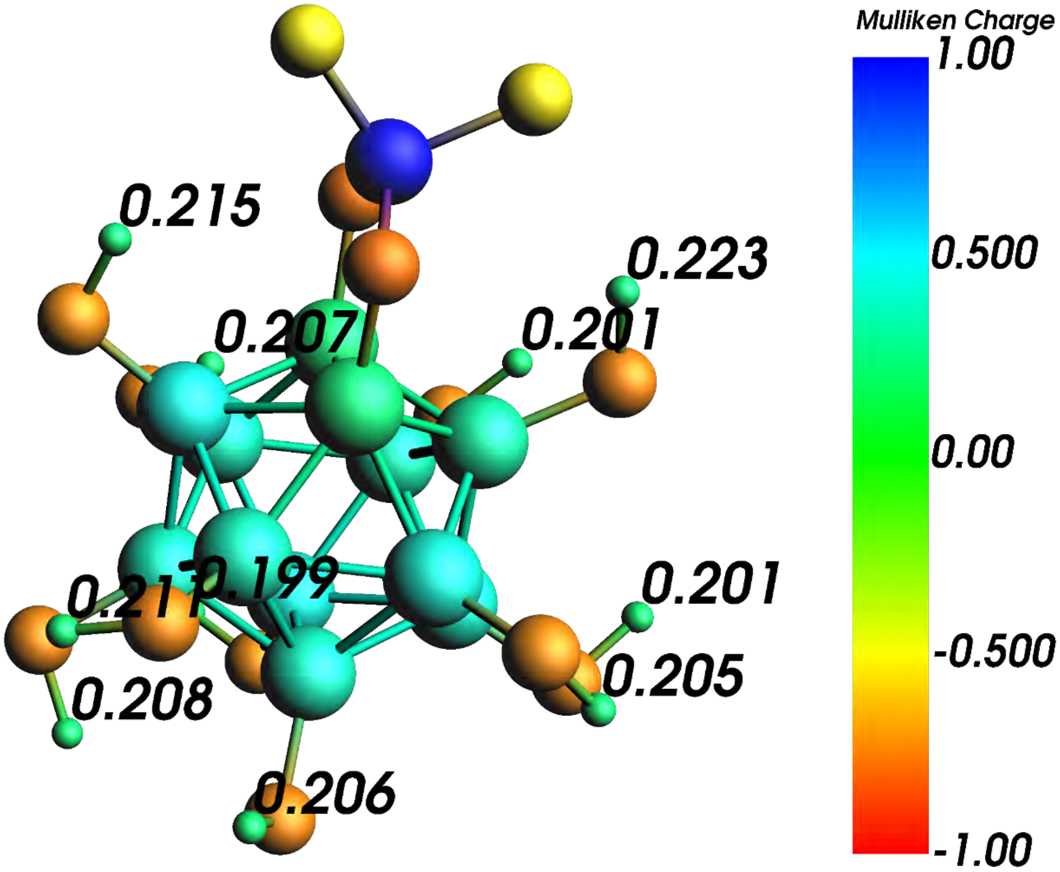

Full Structure Model

Fig. S7 Mulliken charges on boron atoms for full structure model

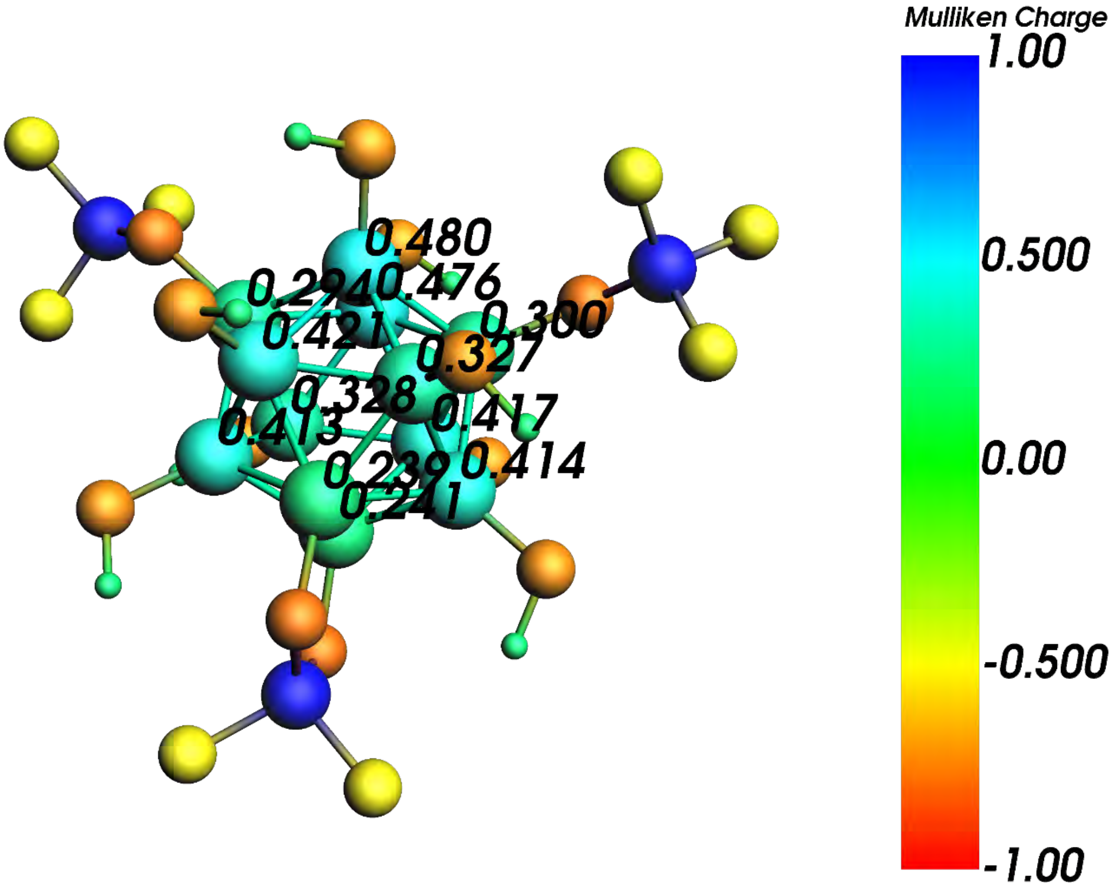

Fig. S8 Mulliken charges on oxygen atoms for full structure model

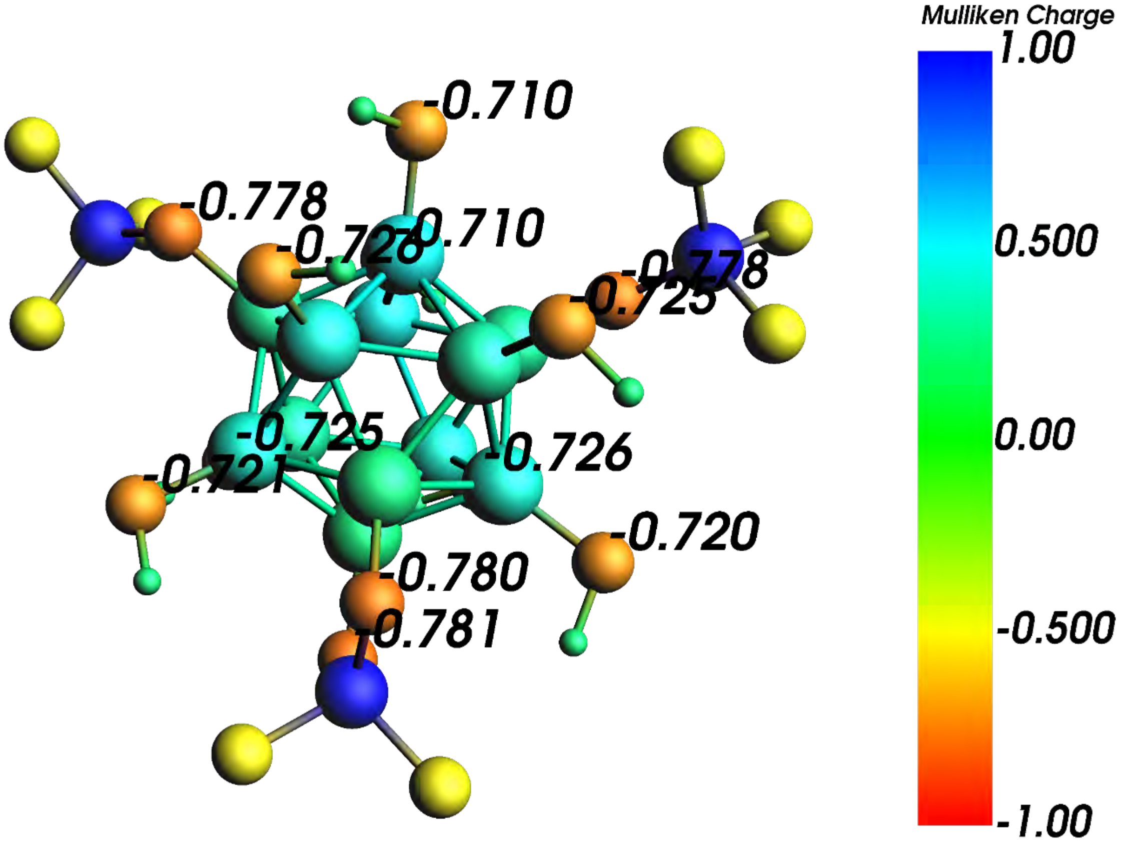

Fig. S9 Mulliken charges on hydrogen atoms for full structure model

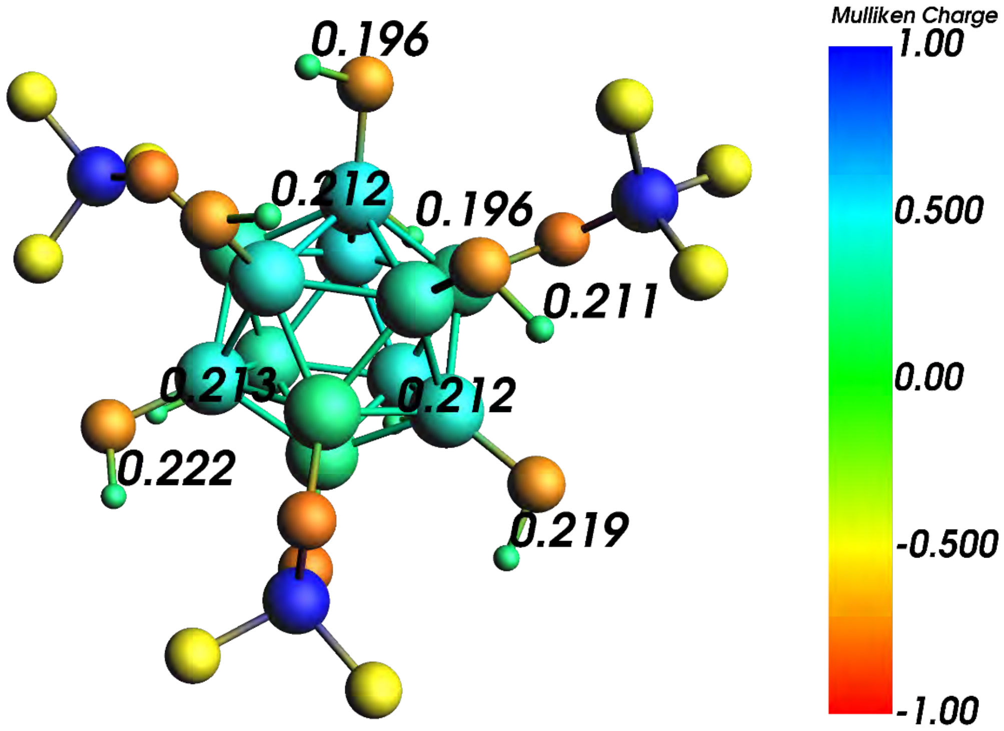

Fig. S10 Rietveld plot for as-synthesized $ZnB_{12}(OH)_{12}$, with green arrows designating the small peaks which corresponding to an unidentified impurity phase

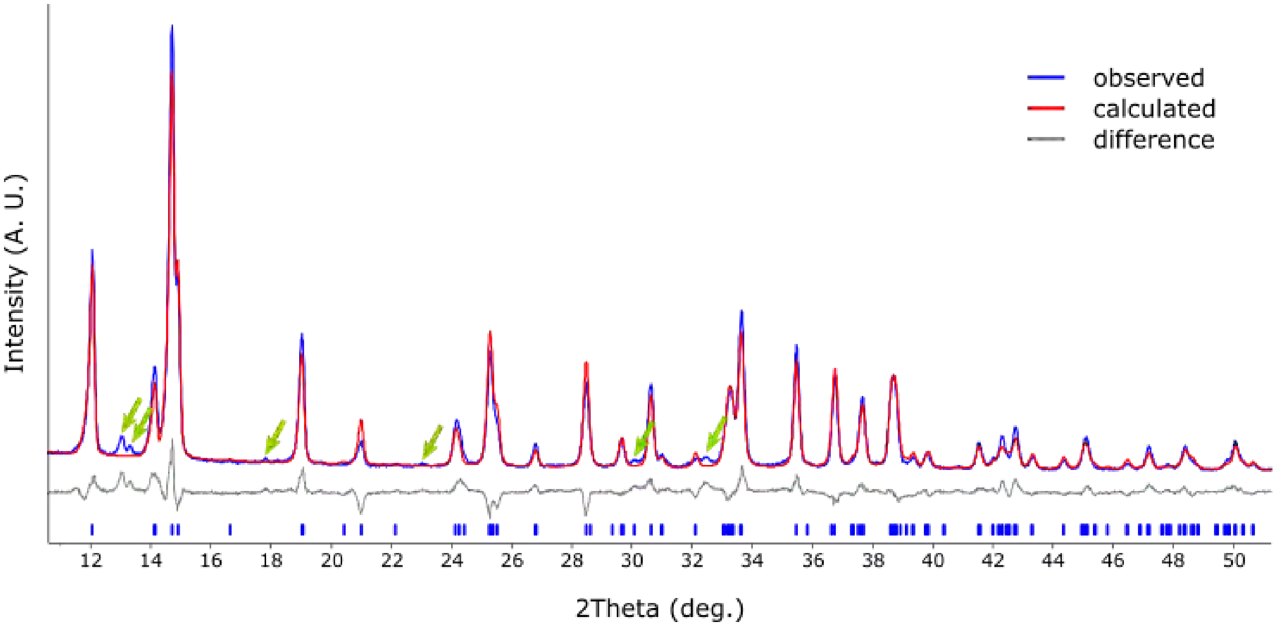

Fig. S11 CIF of $ZnB_{12}F_{12}$, determined through refinement of the powder pattern of as-synthesized $ZnB_{12}(OH)_{12}$

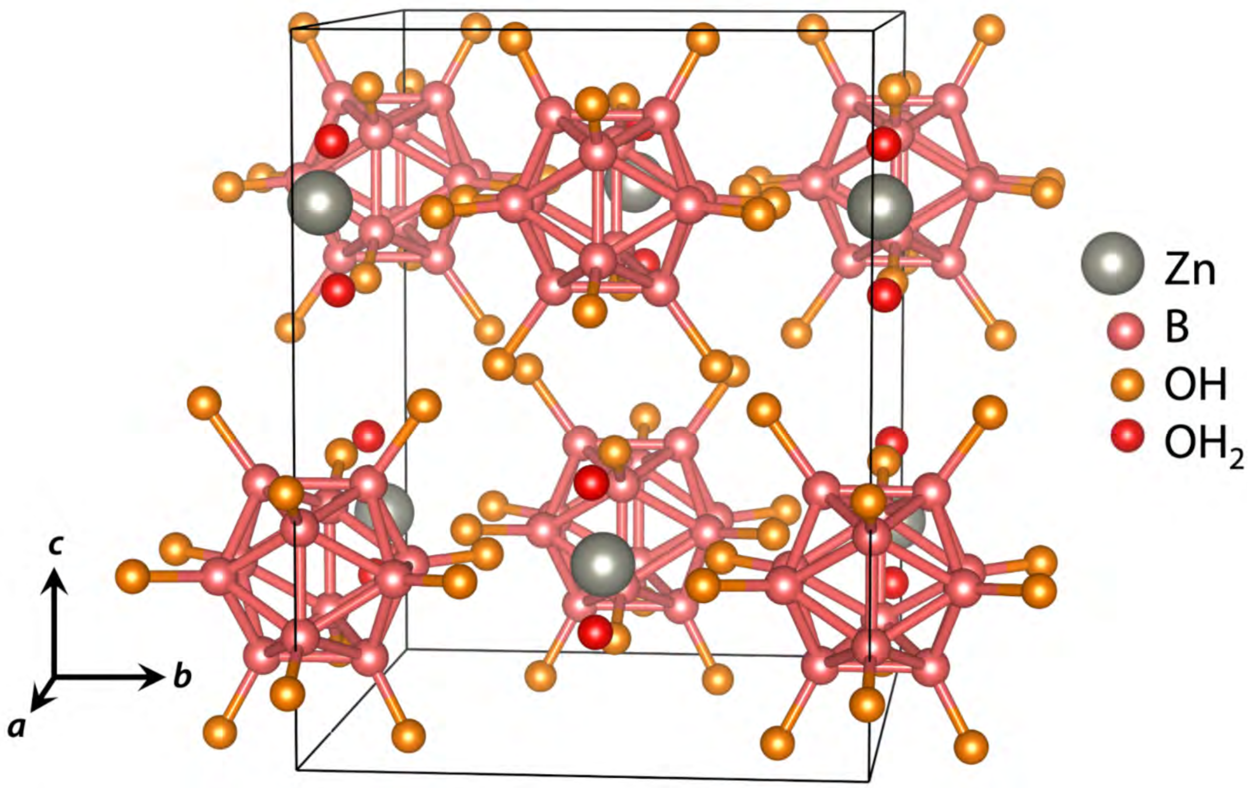

Table S1 Reliability Factors for Refinement

Reliability Factors	
R_{wp}	12.9810467
R_{exp}	3.92036972
R_P	10.0065068
GOF	3.31117921
R_B	8.364317

Table S2 Crystallographic Information for $ZnB_{12}F_{12}$

Lattice Parameters	
Crystal System	Monoclinic
Space Group	C2/m
a	11.8767 (3)
b	9.3221 (2)
c	12.0457 (3)
β	90.082 (6)
Cell Volume	1333.09 (8)
Phase Density	2.2975 (1)

Table S3. Atomic positions for one $ZnB_{12}F_{12}$ moiety (3 zinc ions and one boron cluster)

Listing of all 32 visible atoms:

```
-----------------------------------------------

            Orthogonal Coordinates [Å]

Elmt Label      xor        yor        zor

-----------------------------------------------

 B      B1     2.63149    -9.75698     4.18518

 B     B17      0.90676    -9.84821     4.67223

 B     B19      0.03369   -10.82450     3.44986

 B      B2     1.85292    -9.86305     1.39107

 B     B21      0.11923    -9.95475     1.88065

 B     B22     -0.08030    -9.03219     3.40770

 B      B3     2.82910   -10.67664     2.66046

 B      B4     2.72855    -8.88362     2.61450

 B      B5     1.22149   -11.33509     2.20238

 B      B6     1.53322    -8.37646     3.86045

 B      B7     1.05132    -8.44280     2.14152

 B      B8     1.70567   -11.26850     3.92943
```

F	F10	2.18342	-10.08676	-0.01525
F	F11	4.10309	-11.57334	2.45887
F	F12	3.88287	-8.18605	2.37220
F	F13	1.09575	-12.57833	1.52424
F	F14	1.66027	-7.13308	4.54323
F	F15	0.77258	-7.57612	1.31680
F	F16	1.97333	-12.46135	4.65383
F	F18	0.35561	-9.88652	6.20776
F	F20	-1.06358	-11.84663	3.91789
F	F23	-0.87272	-10.24841	0.84778
F	F24	-1.25316	-8.45772	3.82257
F	F26	6.30118	-9.90268	3.28545
F	F27	5.57406	-9.42550	0.79998
F	F28	7.70649	-7.98381	1.29244
F	F29	5.23820	-6.41326	0.17483
F	F30	6.11578	-6.29628	3.30442
F	F9	3.90345	-9.69886	5.20587
Zn	Zn25	5.76756	-8.22414	1.71021

Zn	Zn31	-3.19209	-8.69805	4.24034
Zn	Zn32	1.62511	-14.38920	3.05961

Water Adsorption Studies

Water isotherms were collected on a Micromeritics 3Flex, and the water uptake in g·g^{-1} units is calculated as [(adsorbed amount of water)/(amount of adsorbent)]. Prior to the water adsorption measurements, water (analyte) was flash frozen under liquid nitrogen and then evacuated under dynamic vacuum at least 3 times to remove any gases in the water reservoir. The temperature was controlled with a Micromeritics ISO Controller. Prior to measurement, the sample was activated under dynamic vacuum on SmartVapPrep (SVP) at 120 °C for 24 hours.

Fig. S12 H_2O sorption isotherm for an activated sample of $ZnB_{12}(OH)_{12}$

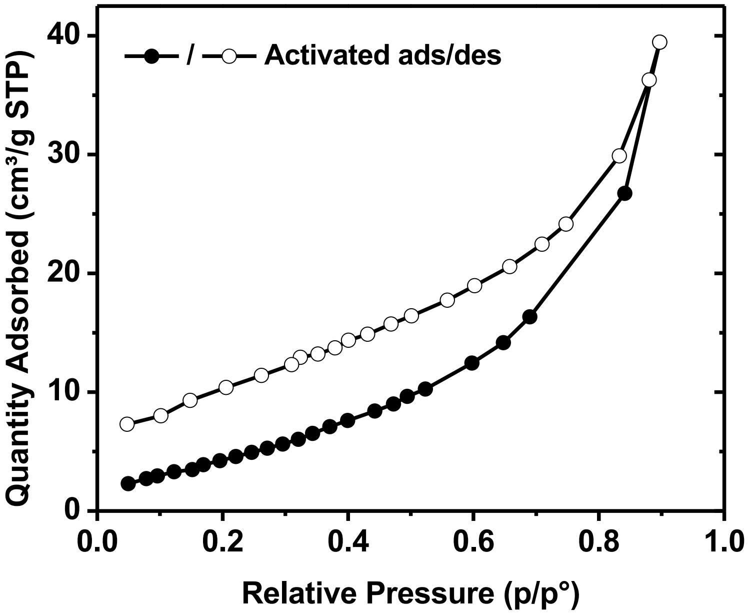

Rehydration in Humidity Chamber

50 mg of freshly activated material was placed on a weigh boat on top of a stand in an airtight chamber. The bottom of the chamber was lined with large filter papers and then filled with water to create a humid environment. The humidity within the chamber was measured to be 85% RH with a SmartPro Digital Hygrometer. The sample was left in the saturated chamber for 48 h and then removed, lyophilized and the PXRD pattern was measured. The sample was then returned to the chamber for 6 more days and the analysis was repeated, showing negligible changes in the PXRD pattern.

Fig. S13 PXRD patterns at various time points of activated $ZnB_{12}(OH)_{12}$ in a humidity chamber

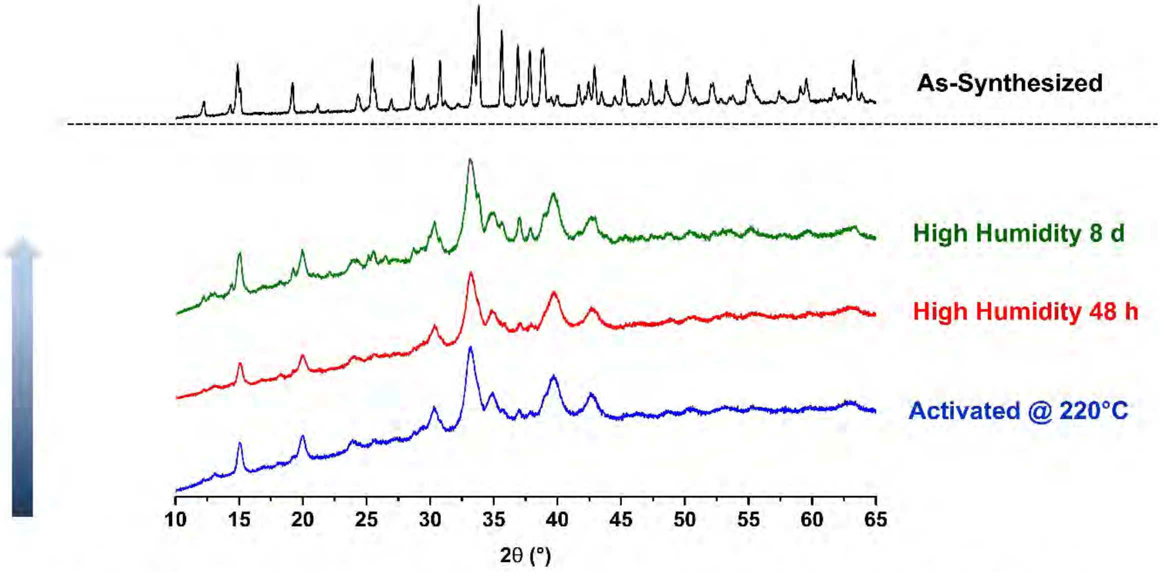

Rehydration in H_2O

35 mg of freshly activated material was stirred as a slurry in 10 mL MilliQ H_2O. After 48 hours, the sample was centrifuged, lyophilized, and then the PXRD pattern was measured. It was then returned to 10 mL of fresh MilliQ H_2O for 3 more days and then analyzed in the same manner, showing full reversion back to the as-synthesized pattern, except for the presence of a small peak at 20° (marked with an asterisk).

Fig. S14 PXRD patterns at various time points of activated $ZnB_{12}(OH)_{12}$ stirred in H_2O

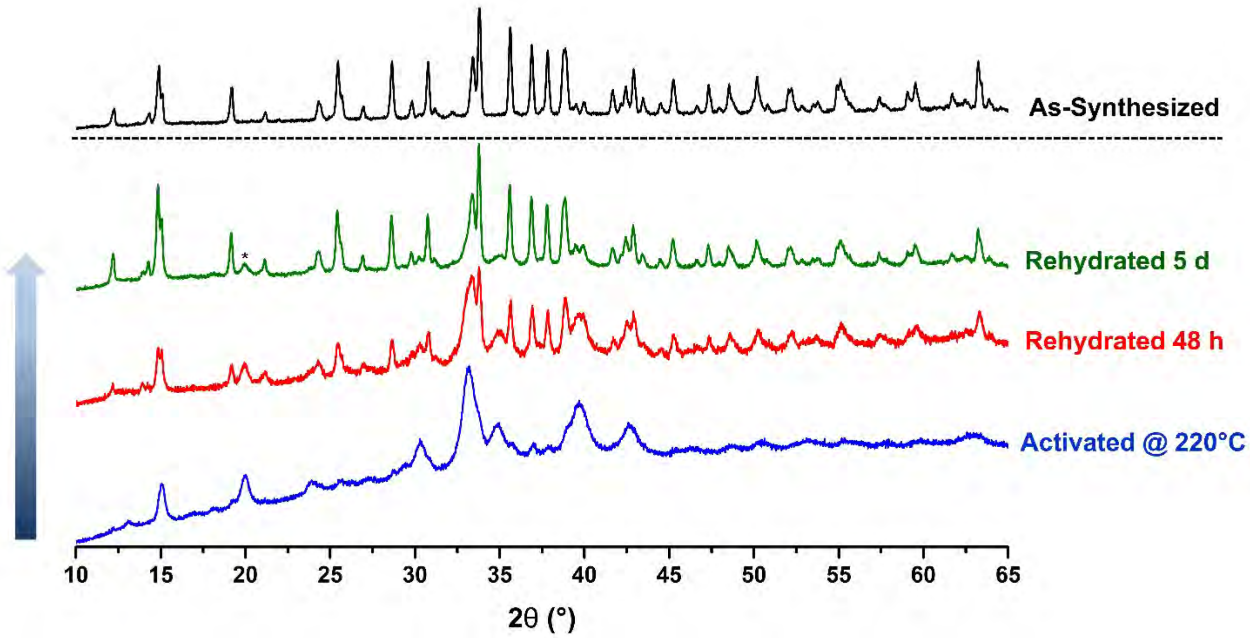

Solvent Exchange with Acetone

16 mg of as-synthesized material was vigorously stirred as a slurry in 5 ml of dry acetone. Every 24 hours the sample was centrifuged, the solvent was removed, and a fresh portion of acetone was added. After 72 hours, the sample was centrifuged, the powder was air-dried overnight, and the PXRD pattern and TGA were measured.

Fig. S15 PXRD patterns of starting material and product after attempting solvent exchange with acetone

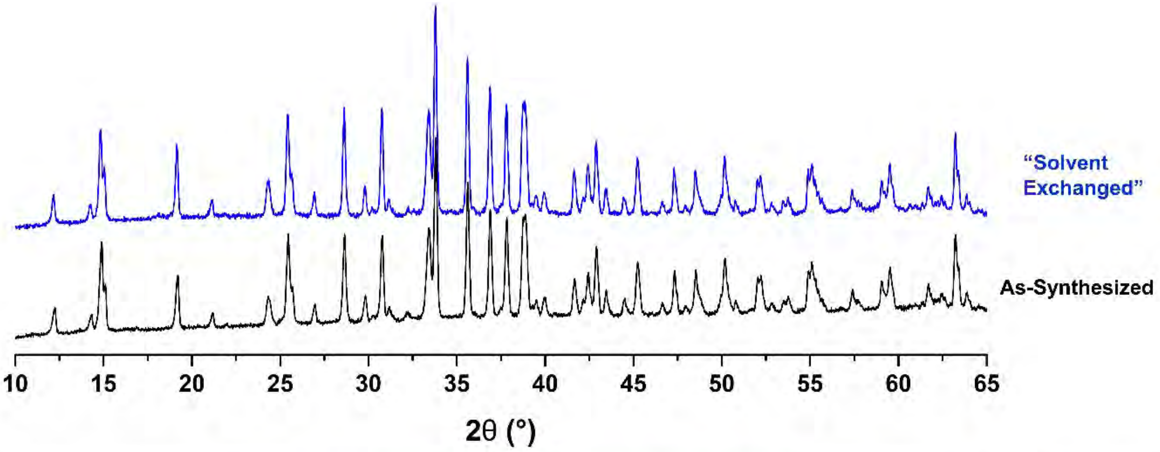

Fig. S16 TGA of material after attempted solvent exchange with acetone

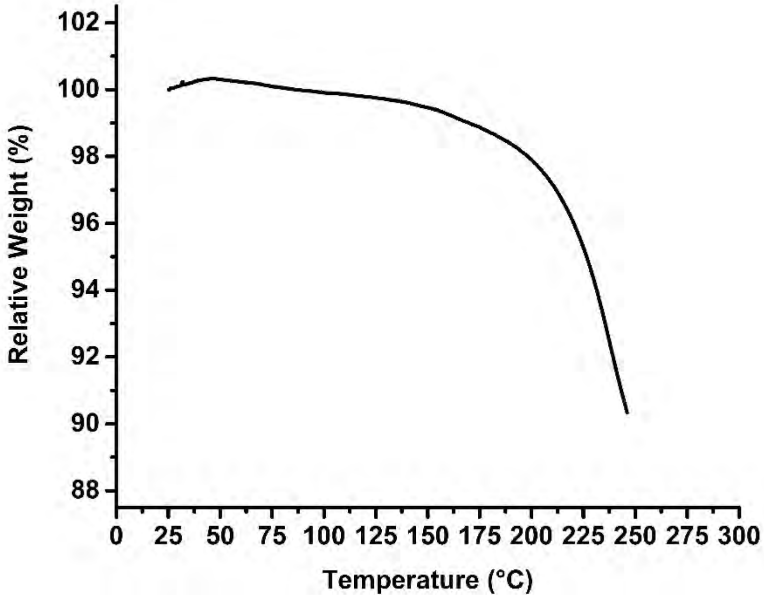

Nitrogen adsorption isotherms

N_2 isotherms were collected at 77 K on a Micromeritics Tristar II 3020. Prior to measurement, the as-synthesized sample was soaked in acetone, washed with acetone, and dried under vacuum at 80 °C for 24 h. Then the sample was activated under dynamic vacuum on SmartVapPrep (SVP) at 120 °C for 24 h. No porosity was observed.

Fig. S17 N_2 adsorption isotherms for as-synthesized (left) and activated (right) samples